



39 patterns (Saros et al., 2019), as well as impacts on water availability, climate, and ocean
40 and atmospheric dynamics that have environmental and climate consequences far beyond
41 the polar regions (IPCC, 2022).

42 The Little Ice Age (LIA; 1300-1900 CE) has been defined as the last period with
43 widespread glacier expansion (Kjær et al., 2022). Greenland GICs have lost 499 Gt of ice
44 from end of LIA to 2021 (Carrivick et al., 2023). The rate of loss of GICs has increased
45 since the 1990s (Bölch et al., 2013; Larocca et al., 2023), with recent trends indicating an
46 acceleration in mass loss from 27.2 ± 6.2 Gt/yr (February 2003–October 2009) to $42.3 \pm$
47 6.2 Gt/yr (October 2018–December 2021) (Khan et al., 2022). Warming rates have been
48 higher in West Greenland than in the East since the end of the LIA (Hanna et al., 2012).
49 As a result, the loss of ice from Greenland's GICs has been more pronounced in its western
50 fringe, where warmer conditions have been associated with the positive phase of the
51 North Atlantic Oscillation (NAO), resulting in a West-to-East warming gradient (Bjørk et
52 al., 2018). Historical records reveal varying trends in GICs over the past two centuries.
53 Aerial images and satellite data indicate that GICs in the West Greenland remained
54 relatively stable, maintaining their extent from the mid-19th century until the mid-20th
55 century, after which they experienced rapid retreat (Weidick, 1994; Leclerq et al., 2012).
56 For instance, Citterio et al. (2009) observed a reduction in glacier area of approximately
57 20% from the LIA to 2001. Other estimates suggest a 48% loss in GICs area in Southern-
58 Western Greenland since the maximum extent of LIA up to 2019 (Brooks et al., 2022).

59 The recent evolution of the GICs has been reconstructed using historical aerial images
60 and satellite records (Leclerq et al., 2012; Yde and Knudsen, 2007; Citterio et al., 2009;
61 Bjørk et al., 2018; Larocca et al., 2023). Geospatial techniques, such as the inference of
62 the Equilibrium Line Altitude (ELA), have also been utilized (Brooks et al., 2022;
63 Carrivick et al., 2023). However, aerial and satellite images provide temporal data over
64 centuries and decades and geospatial methods neglect ice-flow physics and do not account
65 for glacier dynamics. Based on the distribution of moraines and unvegetated trimlines in
66 Central-Western Greenland, some authors suggested that the Late Holocene maximum
67 glacier extent occurred around the LIA (Humlum, 1999). However, cosmic ray exposure
68 (CRE) dating of erosive and depositional glacial records indicates that the maximum ice
69 extent (MIE) of the Late Holocene did not occur during the LIA in many areas in Western
70 Greenland but during the Medieval Warm Period (MWP; 950 to 1250 CE) (Young et al.,
71 2015; Jomelli et al., 2016; Schweinsberg et al., 2019).

72 Evidence from physical-based modelling of the GICs recession during the Holocene
73 remains limited compared to those near the GrIS (i.e., Cuzzzone et al., 2019; Briner et al.,
74 2020). Holocene reconstructions of GrIS extent based on physical modelling, guided by
75 geomorphological evidence, provide valuable insights into the paleoclimate conditions
76 that led to the MIE of the Late Holocene and subsequent recession (Simpson et al., 2009;
77 Lecavalier et al., 2014; Cuzzzone et al., 2019), facilitating comparisons of past and future
78 glacier responses to climate change (Briner et al., 2020). Physical-based ice-flow
79 modelling relying on full-Stokes equations are computationally intensive at high



80 resolution (sub-kilometer) for long-term paleo glacier simulations and model parameter
81 calibrations (Jouvet et al., 2022). Simplified models such as the hydrostatic Shallow Ice
82 Approximation (SIA) and the Shallow Shelf Approximation (SSA) tend to overestimate
83 ice velocities near glacier margins and underestimates velocities in deep glaciated areas,
84 respectively. An emulator based on a convolutional neural network (CNN), trained with
85 high-order ice flow equations, offers reduced computational costs while maintaining
86 accurate ice thickness estimates comparable to those obtained through high-order
87 equations (Jouvet, 2023a).

88 The future recession of Greenland GICs compared to the long-term Holocene fluctuations
89 is poorly understood. Here, we calibrate and validate the Instructed Glacier Model (IGM)
90 (Jouvet et al., 2023a), a glacier evolution model based on a CNN emulator to estimate ice
91 flow, to reconstruct the MIE of the Late Holocene in an extended glacier area in the
92 Eastern Nuussuaq Peninsula (Central-Western Greenland). This area has CRE records
93 available for the outermost glacier moraine complexes but the paleoclimate conditions
94 causing these glacier oscillations are not yet known in detail (D'andrea et al., 2011; Biette
95 et al., 2019; Jomelli et al., 2016; Schweinsberg et al., 2019; Osman et al., 2021).
96 Employing IGM allows us to reconstruct glaciers in high (90 m) resolution based on high-
97 order equations (Jouvet, 2023a), demonstrating the methodology's capabilities for glacier
98 modeling at regional scales. Future glacier evolution is modeled under the CMIP6 SSP2-
99 4.5 and SSP5-8.5 scenarios, from present and steady-state glacier conditions to the year
100 2100. We compared the projected ice loss trend against the reconstructed MIE of the Late
101 Holocene to the present-day ice loss trends, extending glacier records from decades to
102 millennia and placing present and future glacier shrinkage within a long-term Holocene
103 perspective.

104 The objectives of this work are to (i) reconstruct past glaciers under different climate
105 conditions, (ii) determine past and future climate conditions influencing the MIE of the
106 Late Holocene and future glacier recession, (iii) quantify future glacier retreat trends, and
107 (iv) compare future ice loss trends with the rate of ice loss from the MIE of the Late
108 Holocene to the present.

109 **2. Study area**

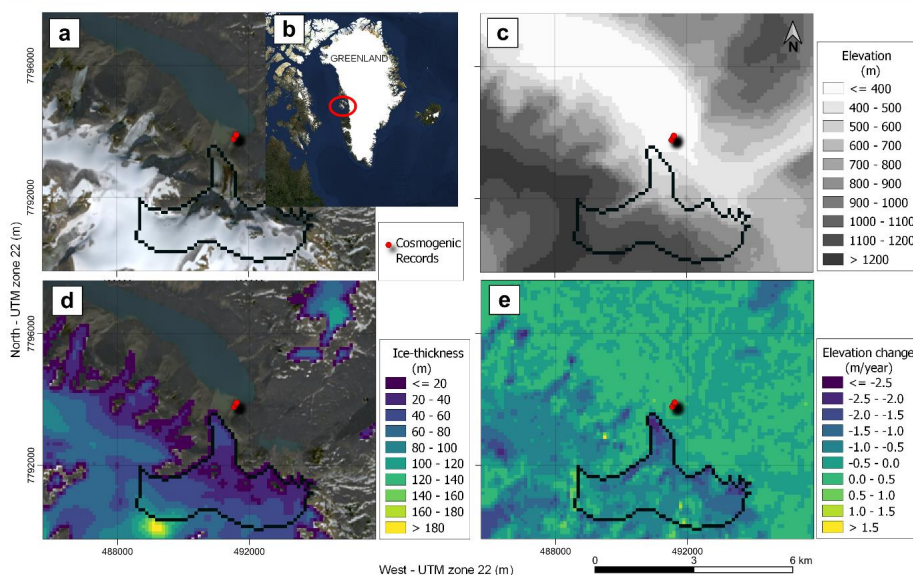
110 This study focuses on a land-terminating glacier area in the Nuussuaq Peninsula, Central-
111 West Greenland (Figure 1). This peninsula extends from the onshore Disko (South) to
112 Svartenhuk Halvo (North). Nuussuaq Peninsula includes several mountain glaciers and
113 ice caps connected to the GrIS that surrounds its eastern flank. Our study focuses on a
114 glacier area in the Eastern Nuussuaq Peninsula, with elevations ranging from 400 to 1200
115 meters above sea level (m a.s.l.) (Figure 1).

116 Present-day climate conditions are characterized by a polar maritime climate, becoming
117 more continental toward the inland areas and GrIS (Humlum, 1999). Moist air masses
118 from the Davis Strait influence the climate during summer, with continental polar air
119 influences during the winter (Ingolfsson et al., 1990). Prevailing winds in the region



120 typically come from the East and North-East, except during the summer months, when
121 Southerly and Southern-Western winds prevail (Humlum, 1999). The relief configuration
122 exposes Disko Bugt to cyclogenetic activity and moist airflow, resulting in decreased
123 precipitation from the peripheral coastal areas towards the GrIS (Weidick and Bennike,
124 2007). The nearest research station with meteorological and snow observations is the
125 Arctic station, at coastal Disko Island (Central-Western Greenland). Here, the
126 accumulated annual precipitation is 436 mm (1991–2004 period) (Hansen et al., 2006).
127 The mean annual temperature (MAAT) is -4°C (1961–1990 period), with a lapse rate of
128 around 0.6°C per 100 m (Humlum, 1998). At Arctic station, the snow season typically
129 extends from September to June, with maximum snow accumulations of around 50 cm
130 (Bonsoms et al., 2024).

131 The present-day landscape in Central-West Greenland is characterized by the presence of
132 glaciers, which have also intensely shaped the relief in ice-free areas in the past. Today,
133 environmental dynamics in these areas is strongly influenced by periglacial processes
134 under a continuous permafrost regime (Humlum, 1998; Christiansen et al., 2010) that
135 reshape the geological setting made of clastic sediments from the Mid-Cretaceous to the
136 Palaeogene (Pedersen et al., 2002). The strong glacial imprint in the landscape of the
137 peninsula results from a complex glacial history, which is not yet known in detail.
138 Following the LGM, the GrIS underwent a significant retreat during Termination-1 and
139 exposed the coastal regions in Central-West Greenland (Briner et al., 2020). As in other
140 regions across Greenland, the Early Holocene was characterized by warm temperatures
141 that led glaciers to retreat (Leger et al., 2024). In the Nuussuaq Peninsula, CRE records
142 reported the onset of glacial retreat by ca. 10 ka (O'Hara et al., 2017). The minimum GrIS
143 extension occurred from ca. 5 to 3 ka cal BP, when GrIS margins retreated by ca. 150 km
144 from present-day terminus position (Briner et al., 2016), which explains the lack of glacial
145 records corresponding to the Early-Mid Holocene in the peninsula (Kelly and Lowell,
146 2009; O'Hara et al., 2017). According to several absolute dating methods in different
147 natural records, the Nuussuaq Peninsula GICs grew between approximately 4.3 and 2 ka
148 and reached several glacier culminations during the past millennium before the LIA
149 (Schweinsberg et al., 2017; 2019). The internal and external moraine complexes in the
150 area reported CRE ages of 1130 ± 40 and 925 ± 80 CE, respectively (Young et al., 2015).
151 These ages are consistent with other CRE ages obtained in Central-Western Greenland
152 for the most external recent moraine complexes, indicating that the late MWP glacier
153 expansion was the largest of the Late Holocene (Jomelli et al., 2016; Schweinsberg et al.,
154 2019)



155

156 **Figure 1.** Location of the reconstructed glacier and CRE ages (red points) used in this
 157 work (a). Location of the study area within Greenland (b). Glacier delimitation is based
 158 on Randolph Glacier Inventory (RGI6). The base map is a Sentinel-2 image from
 159 <https://s2maps.eu/> (2022). Elevation map of the study area from a Digital Elevation
 160 Model Copernicus DEM GLO-90 (2010-2015) (c). Average ice thickness (m) (2018-
 161 2022) from Millan et al. (2022) (d). Elevation changes average values (m/year) between
 162 2000-2019 (Hugonnet et al., 2021) (e).

163 3. Data

164 3.1 Pre-processing glacier data downloading

165 The data used to force and validate the IGM is detailed at Table 1. Topography data were
 166 obtained from a Copernicus Digital Elevation Model (DEM) with a resolution of 90
 167 meters (COPERNICUS DEM GLO-90). In-situ mass balance records in the study area
 168 are scarce and fieldwork is challenging. However, recent advancements in global-scale
 169 mass balance, satellite imagery, and ice thickness estimates have enabled the validation
 170 of the glacier model. We compared the ice thickness estimates from Farinotti et al. (2019),
 171 which are the output from an ensemble of five models (HF-model, GlabTop2, OGGM,
 172 GlabTop2 IITB version, and an unnamed model), with those from Millan et al. (2022),
 173 which are derived from numerical modeling based on SIA and data obtained from a
 174 constellation of remote sensing products (Sentinel-1/ESA, Sentinel-2/ESA, Landsat-
 175 8/USGS, Venus/CNES-ISA, Pléiades/Airbus D&S). Glacier mask outlines were acquired
 176 from the Randolph Glacier Inventory Version 6 (RGI6.0). Elevation change rate (dh/dt)
 177 data were obtained from Hugonnet et al. (2021).



178 The climate variables required to run the IGM model are monthly accumulated
 179 precipitation ($\text{kg m}^{-2} \text{ yr}^{-1}$), monthly average air temperature ($^{\circ}\text{C}$), and monthly air
 180 temperature standard deviation ($^{\circ}\text{C}$) from the nearest pixel to the glacier. We utilized the
 181 GSWP3- W5E5 monthly dataset at a spatial resolution of $0.5^{\circ} \times 0.5^{\circ}$, which combines the
 182 Global Soil Wetness Project phase 3 dataset with the bias-adjusted ERA5 reanalysis
 183 dataset (Cucchi et al., 2020). Future glacier changes are modeled based on bias-corrected
 184 monthly accumulated precipitation and monthly average air temperature CMIP6 multi-
 185 model mean ($n=33$) for SSP2-4.5 and SSP5-8.5 (2020 to 2100) at a spatial resolution of
 186 0.25° (Thrasher et al., 2022), subtracted at the nearest grid point of the glaciers. Months
 187 are aggregated into seasons as follows: September, October, November (Autumn), March,
 188 April and May (Spring), December, January and February (Winter), June, July and August
 189 (Summer). Data were downloaded using Open Global Glacier Model (OGGM) model
 190 (<https://oggm.org/>) (Maussion et al., 2015) shop module of IGM (Jouvet et al., 2023),
 191 except for CMIP6 projections (Thrasher et al., 2022) and ice thickness estimates (Farinotti
 192 et al., 2019).

193 **Table 1.** Characteristics of the datasets employed for forcing, calibrating, and validating
 194 the IGM.

Description	Name	Spatial resolution	Database Date	Source
DEM	Copernicus DEM GLO-90	90 m	2010-2015	https://spacedata.copernicus.eu/documents/20126/0/CSC_DA_ESA_User_Licence_2021_11_17.pdf
Ice-thickness (1)	Millan et al. (2022)	100 m	2017-2018	Millan et al. (2022)
Ice-thickness (2)	Farinotti et al. (2019)	25 m	2019	Farinotti et al. (2019)
Baseline climate data	GSWP3_W5E5v2.0	$0.5^{\circ} \times 0.5^{\circ}$	1960-1990	https://data.isimip.org/search/simulation_round/ISIMIP2a/product/InputData/climate_forcing/gswp3-w5e5/
CMIP6 projections	CMIP 6	0.25°	1960-2100	Thrasher et al. (2022)
Dh/dt	Hugonnet et al. (2021)	Glacier (RGI6.0) level	2000-2020	Hugonnet et al. (2021)
Glacier Outline	RGI6.0	Glacier (RGI6.0) level	2003	https://www.glims.org/RGI/

195

196 **3.2 Geomorphological and paleoclimate data**



197 The CRE ages are based on nuclide (^{10}Be) introduced by Young et al. (2015) and refer to
198 the period of the maximum glacier advance of the last warm/cold cycles in the Nuussuaq
199 Peninsula and were used for the paleoclimate modelling purposes of this study. The
200 sampled boulders were obtained from the outer ridge of the moraine and reveal either (i)
201 a period of glacial surge or (ii) a phase of stabilization/stillness during the long-term
202 retreat. However, special caution must be taken when interpreting these ages, as they are
203 not directly indicative of the period of ice occupation but of the timing of stabilization of
204 moraine boulders.

205 Paleoclimate anomalies with respect to the baseline climate were obtained from annual
206 air temperature reconstructions from ice cores of the GrIS and margins of the GrIS
207 provided by Buizert et al. (2018). This data ranges from the Last Glacial Maximum
208 (LGM; $\sim 26\text{-}19$ ka ago) to 2000 CE.

209 **4. Methods**

210 **4.1 Instructed Glacier Model (IGM)**

211 The IGM is a glacier model that simulates ice thickness evolution according to ice mass
212 conservation principles, surface mass balance and ice flow physics (Jouvet et al., 2023a).
213 IGM updates the ice thickness at each time step from ice flow and surface mass balance
214 (SMB) by solving the mass conservation equation. The ice flow is modelled using a CNN
215 model that is trained to satisfy high-order ice flow equations. There are two main
216 parameters that control the strength of the ice flow: the Arrhenius factor (A) that controls
217 the ice viscosity in Glen's flow law (Glen, 1955) and the basal sliding coefficient (c), by
218 the nonlinear sliding Weertman's law (Weertman, 1957).

219 Temperature data is downscaled over the DEM using a reference height and a constant
220 lapse rate of $-0.6^\circ\text{C}/100$ m, while precipitation is downscaled using a vertical gradient of
221 35 mm/100 m. Precipitation is classified as solid ($< 0^\circ\text{C}$) or liquid ($> 2^\circ\text{C}$), with a linear
222 transition between solid and liquid phases. The melting threshold is set to -1°C , and the
223 density of water is fixed at 1000 kg m^{-3} . The SMB is estimated using a monthly positive
224 degree-day (PDD) model (Hock, 2003; Huss, 2008). The PDD is calibrated based on the
225 OGGM v1.6.1 SMB calibration process, which is included in IGM SMB module. OGGM
226 v1.6.1 SMB calibration correct temperature and precipitation biases from climate data
227 and adjust the melt factor (5, in this case) to fit the average glacier geodetic mass balance
228 from January 2000 to January 2020 from Hugonnet et al. (2021). Further details of the
229 OGGM v1.6.1 SMB calibration process are provided in the OGGM documentation
230 (https://oggm.org/tutorials/master/notebooks/tutorials/massbalance_global_params.html
231), whereas the physical basis of IGM is detailed in Jouvet et al. (2022; 2023a).

232 **4.2 Present day glacier calibration and validation**

233 We calibrated the IGM to simulate RGI6.0 area, and ice thickness from available datasets
234 (Farinotti et al., 2019; Millan et al., 2022). The IGM parametrization is performed based
235 on conducting a sensitivity analysis to A and c . These parameters were chosen to optimize



236 IGM and accurately simulate different ice conditions, basal sliding conditions and
237 subglacial hydrology. An ensemble of IGM parameter options was performed over a
238 model run of 1000-years with different temperature perturbations of -0.75°C , -0.5°C , 0°C
239 and $+0.25^{\circ}\text{C}$ with respect to baseline climate (1960-1990) in order to reach long-term ($>$
240 500 years) glacier area steady-state conditions. The range of temperature perturbation was
241 determined through trial and error, which showed that values outside this range of
242 temperature anomalies produced higher discrepancies with respect to the available
243 datasets used for results validation (Figure 3 to 5). A sensitivity analysis was performed
244 on IGM parametrization to simulate cold, temperate, and soft ice conditions by changing
245 A from $34 \text{ MPa}^{-3} \text{ a}^{-1}$, $78 \text{ MPa}^{-3} \text{ a}^{-1}$ (IGM default value) to $150 \text{ MPa}^{-3} \text{ a}^{-1}$. Sliding
246 conditions are parametrized by changing c from $0.01 \text{ km MPa}^{-3} \text{ a}^{-1}$, $0.03 \text{ km MPa}^{-3} \text{ a}^{-1}$
247 (IGM default value), and $0.05 \text{ km MPa}^{-3} \text{ a}^{-1}$. The IGM parametrization is shown in
248 Figures 3 to 5. The remaining parameters were set to the default configuration of the IGM.

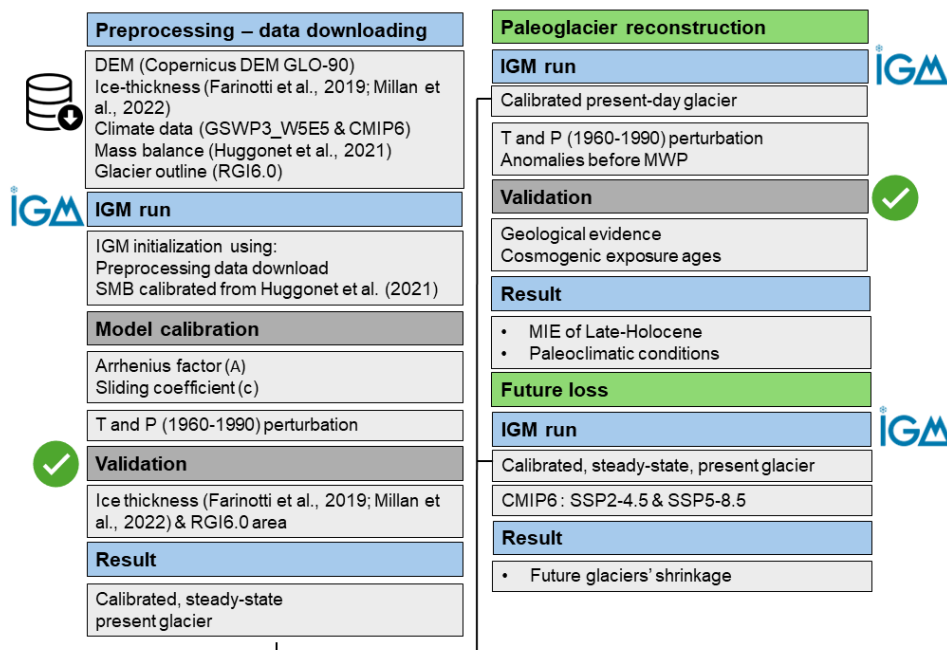
249 The accuracy evaluation of the modeled IGM outputs is based on both area and ice
250 thickness. We calculated (i) the Mean Absolute Error (MAE) between the accumulated
251 glacier ice thickness from Farinotti et al. (2019) and Millan et al. (2022) and the output
252 from IGM; (ii) the glacier area difference between RGI6.0 area and from IGM. To
253 incorporate both area and ice thickness errors, we calculated the bias by multiplying the
254 ice thickness MAE (i) by the area difference (ii).

255 **4.3 Past and future glacier evolution**

256 IGM is forced with the lowest error parameterization option until the glacier area reaches
257 present-day and long-term stable-state conditions. The model is run again 1000-years
258 with an ensemble of different temperature and precipitation values to simulate MIE of the
259 Late Holocene from MWP. The temperature was perturbed over the baseline climate from
260 0 to -1°C by steps of 0.25°C . Precipitation was non-changed (0%) and increased (10%) in
261 order to estimate if high rates of snowfall could compensate warming. MIE of the Late
262 Holocene paleoclimate conditions were determined by calculating the distance between
263 the glacier tongue of the ensemble of simulations and the CRE dates of the outer ridge
264 moraines (Köse et al., 2022). The simulations that match the outer ridge moraines
265 represent the climate conditions before the CRE dates. The present-day glacier area with
266 steady-state conditions is the starting point of the future simulations (Zekollari et al.,
267 2019). Subsequently, the IGM is run from the present day until 2100 using monthly
268 accumulated precipitation and average air temperature CMIP6 multi-model mean SSP2-
269 4.5 and SSP5-8.5 anomalies with respect to the baseline climate, applying additive factors
270 for temperature and multiplicative factors for precipitation (Rounce et al., 2023). Present
271 and future ice thickness anomalies with respect to the MIE of the Late Holocene are
272 calculated by subtracting the difference between the accumulated ice thickness for the
273 MIE of the Late Holocene (i) from the accumulated ice thickness from the present-day
274 (ii) and future ice-loss (iii), dividing by the accumulated ice thickness for the MIE of the
275 Late Holocene (i), and multiplying by 100. The factor of increase under future climate



276 change is calculated by dividing future ice loss anomalies by the present-day ice loss
 277 anomalies relative to the MIE of the Late Holocene.



278

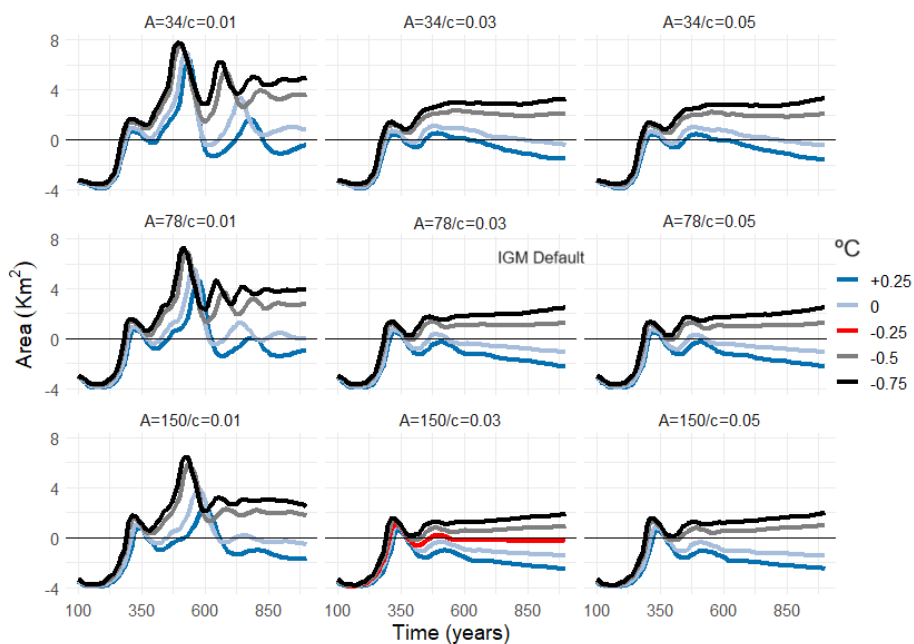
279 **Figure 2.** Flowchart followed for reconstructing past and present glaciers and projecting
 280 their future evolution based on air temperature (T) and precipitation (P).

281 **5. Results**

282 **5.1 IGM parametrization and calibration**

283 For most IGM parametrizations, glacier growth occurred until 350 to 600 years of spin-
 284 up. The latest year of the spin-up simulation is subsequently validated against ice
 285 thickness estimates (Farinotti et al., 2019; Millan et al., 2022). The error metric values for
 286 ice thickness and area resulting from the IGM calibration and parametrization process are
 287 shown in Figure 3 to 5. The most favorable range for achieving accurate results for
 288 present-day glaciers is a perturbation range of temperature from 0°C to -0.5°C with respect
 289 to the baseline climate (Figure 3 to 5). The largest errors in ice thickness and glacier area
 290 were observed for the $A = 34 \text{ MPa}^{-3} \text{ a}^{-1}$ and $c = 0.01 \text{ km MPa}^{-3} \text{ a}^{-1}$ IGM configuration.
 291 This configuration tended to overestimate ice thickness for both global-scale ice thickness
 292 references (Figure 4 and 5). Additionally, using the default configuration and reducing
 293 the temperature to $< -0.5 \text{ °C}$ over the baseline climate led to overestimations of ice
 294 thickness.

295



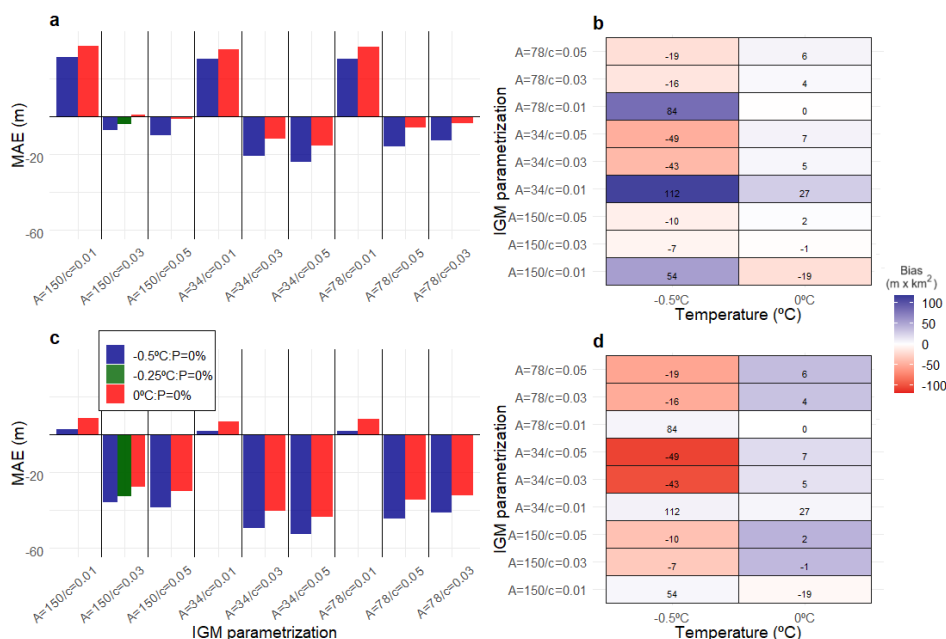
296

297 **Figure 3.** Difference from the RGI6.0 area and IGM outputs within a 1000-years spin-
298 up. Data is grouped by changes in temperature (colors), A and c options (boxes). The
299 selected configuration ($A = 150 \text{ MPa}^{-3} \text{ a}^{-1}$ and $c = 0.03 \text{ km MPa}^{-3} \text{ a}^{-1}$, -0.25°C with
300 respect to the baseline climate) is shown in red color.

301

302

303



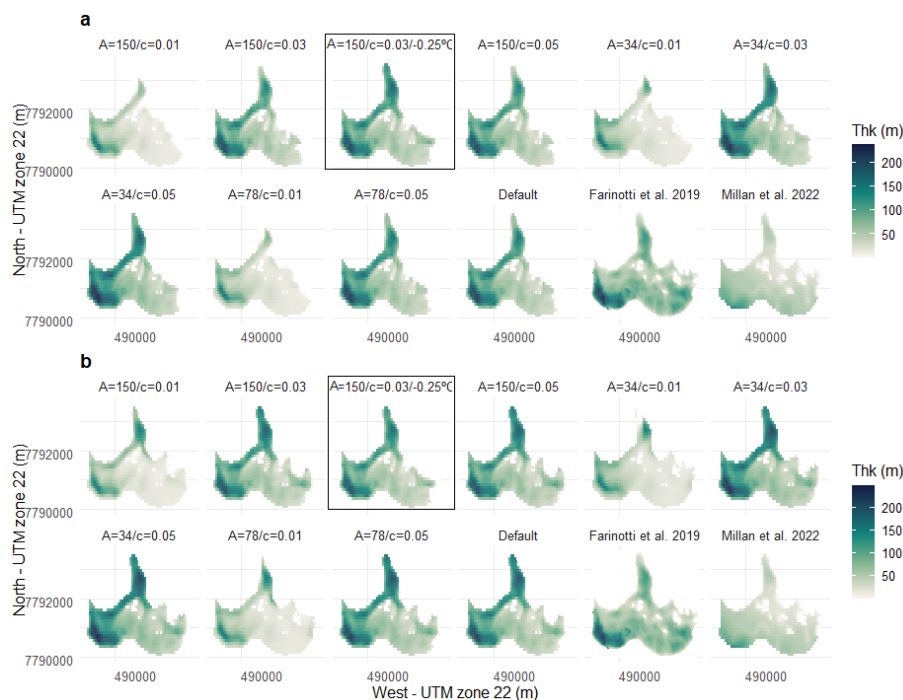
304

305 **Figure 4.** Ice thickness MAE between Farinotti et al. (2019) and IGM outputs after spin-
 306 up with different A and c parametrizations and perturbations of temperature (a). The
 307 selected configuration is shown with green color. Ice thickness MAE values from Figure
 308 4 (a) multiplied by the difference between the RGI6.0 area and the IGM outputs (bias)
 309 for different A and c parametrizations and perturbations of temperature (b). Figure 4 (c)
 310 and (d) are the same as Figure 4 (a) and (b), respectively, but for ice thickness estimates
 311 from Millan et al. (2022).

312 Trial and error parametrizations of A and c revealed that optimal results were achieved
 313 for $A = 150 \text{ MPa}^{-3}\text{a}^{-1}$ and $c = 0.03 \text{ km MPa}^{-3} \text{ a}^{-1}$. These outputs of the IGM align with
 314 Farinotti et al. (2019). However, both IGM ice thickness and Farinotti et al. (2019)
 315 overestimate ice thickness compared to Millan et al. (2022) (Figures 4 and 5). Setting A
 316 $= 150 \text{ MPa}^{-3}\text{a}^{-1}$ and $c = 0.03 \text{ km MPa}^{-3} \text{ a}^{-1}$, with a slight variation of temperature (-0.25
 317 °C) over the baseline climate, resulted in very similar accumulated ice thickness to
 318 Farinotti et al. (2019) (MAE = 4 m; Figure 4a), a minimal RGI6.0 area bias (Figure 3 and
 319 4b), and very stable-state glacier conditions for > 500 years (Figure 3). This configuration
 320 also minimized errors against the Millan et al. (2022) dataset (MAE = 24 m) (Figure 4c).
 321 Thus, glacier reconstruction and projection are based on this parametrization option.

322

323



324

325 **Figure 5.** Average ice thickness data from Farinotti et al. (2019) and Millan et al. (2022),
 326 along with examples of IGM configuration options using different A and c parameters for the selected configuration (highlighted with a black square), are shown for a temperature
 327 of 0°C with respect to the baseline climate (a) and a temperature of -0.5°C with respect to
 328 the baseline climate (b). The ice thickness values of IGM shown are the result of steady-
 329 state glacier conditions.
 330

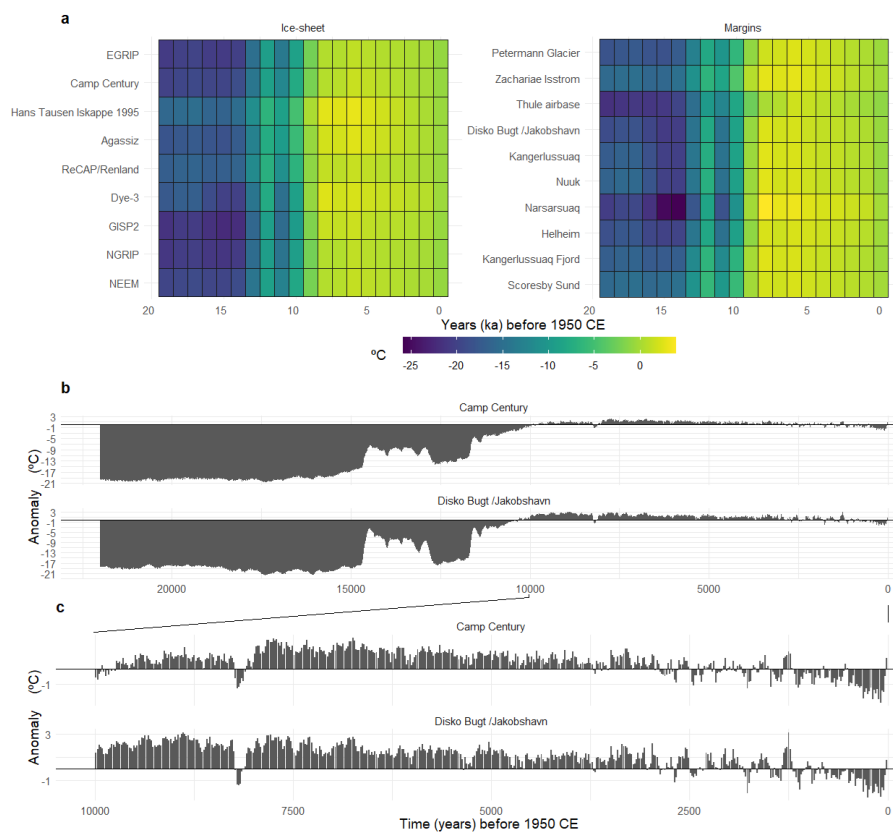
331 5.2 Late Holocene maximum glacier extension and paleoclimatic conditions

332 The temperature evolution from the LGM to 2000 CE, as reconstructed from GrIS ice
 333 cores and Greenland margins (Buizert et al., 2018), is shown in Figure 6. The Camp
 334 Century and Disko Bugt/Jakobshavn ice cores exhibit similar temperature trends
 335 compared to the baseline climate period, although they display larger temperature
 336 anomalies, with the warmest conditions recorded during the Holocene Warm Period
 337 (HWP; ~ 9-5 ka ago) (up to 3°C with respect to the baseline climate period). A long-term
 338 cooling trend is detected for the Late Holocene, with moderate anomalies and high yearly
 339 oscillations of around ± 1 °C between the Dark Ages Cold Period (~ 400 to 765 CE;
 340 Helama et al., 2017) and the MWP for Disko Bugt/Jakobshavn (Figure 6). However,
 341 colder temperatures are found in the Camp Century ice core. For both locations, the
 342 coldest temperature anomalies of ca. -2°C compared to the baseline climate are found
 343 during the LIA.

344



345



346

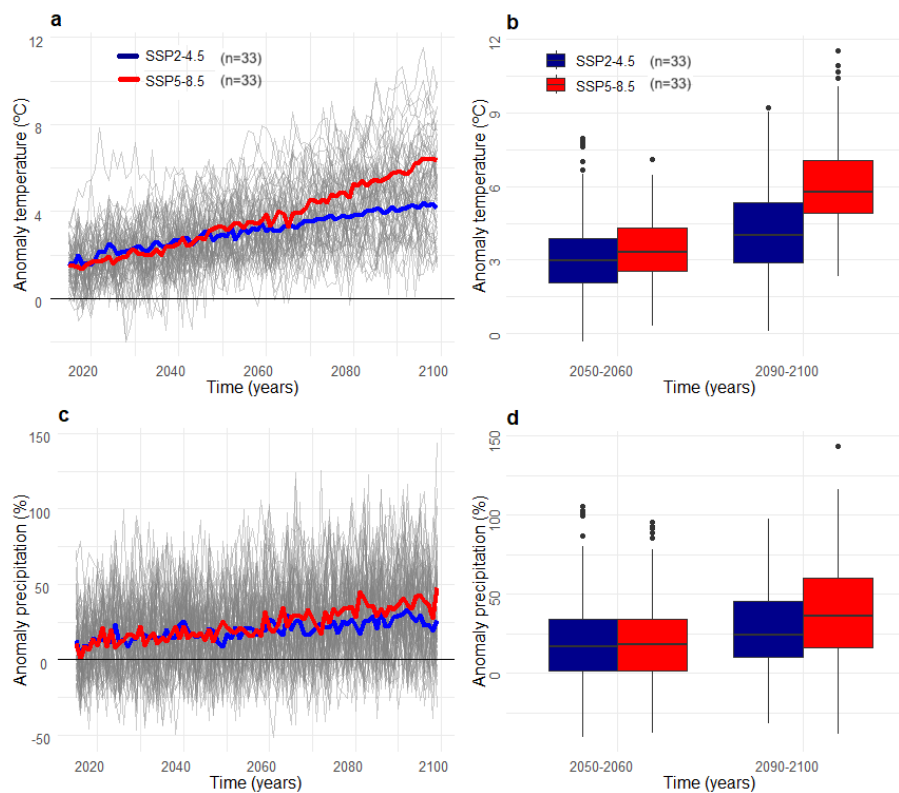
347 **Figure 6.** Air temperature anomalies from the LGM period to the present reconstructed
 348 from ice-core records of the GrIS and Greenland margins (a). Air temperature anomalies
 349 from the ice cores near to the glacier reconstructed in Central-Western Greenland (Camp
 350 Century and Disko Bugt/Jakobshavn) (b). The black squares highlighted in (a) correspond
 351 to the specific locations shown in (b). Air temperature anomalies since 10 ka to 1950 (c).
 352 Air temperature anomalies are calculated by the difference between the average annual
 353 air temperature from the baseline climate (1960-1990 period) and the annual air
 354 temperature for each location. Data were obtained from the reconstruction available from
 355 Buizert et al. (2018).

356 Future CMIP6 SSP2-4.5 and SSP5-8.5 anomalies with respect to the baseline climate are
 357 shown in Figure 7. The temporal evolution of temperature follows a similar warming rate
 358 for both scenarios until 2040, after which there is an acceleration of warming for SSP5-
 359 8.5. The increase in temperature relative to the baseline climate for SSP2-4.5 is 3.1°C by
 360 2050 and 4.2°C by 2100, whereas for SSP5-8.5, is 3.4°C by 2050 and 6.1°C by 2100.
 361 Thus, CMIP6 (SSP2-4.5 and SSP5-8.5) anomalies with respect to the baseline climate are
 362 similar to HWP for 2050 but higher by a factor of three for SSP5-8.5 by 2100 (Figure 6).



363 Precipitation also shows an increase with respect to the baseline climate, which is more
364 pronounced for SSP5-8.5 towards the end of the 21st century. SSP2-4.5 precipitation
365 anomalies with respect to the baseline climate are +20% by 2050, increasing to +26% by
366 2100. For SSP5-8.5, precipitation increases by +20% by 2050 and +38% by 2100.

367 For the 2050-2060 period, summer temperatures are projected to range from 2°C under
368 SSP2-4.5 to 3°C under SSP5-8.5. For the 2090-2100 period, winter temperatures are
369 projected to range from 5°C under SSP2-4.5 to 8°C under SSP5-8.5 (Figure S1).
370 Regarding snowfall and for the 2050-2060 period, SSP2-4.5 and SSP5-8.5 projects
371 anomalies of 12% and 16 %, respectively (Figure S2 and S3). For the 2090-2100 period,
372 anomalies with respect to the baseline climate are 18 % and 22% for SSP2-4.5 and SSP5-
373 8.5, respectively. Other months show decreases in snowfall except for Spring, which
374 shows a 3% increase for both SSP5-8.5 and SSP2-4.5 scenarios for 2050-2060 and 2090-
375 2100 periods.



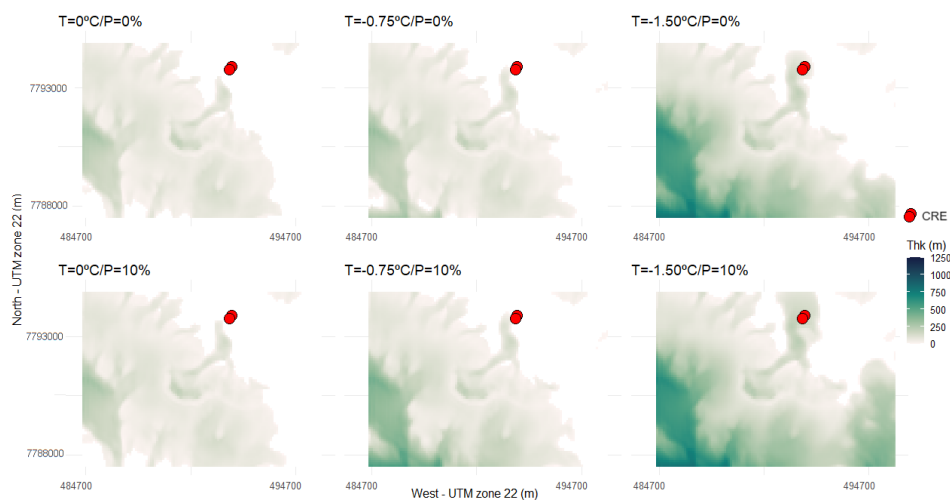
376

377 **Figure 7.** Temporal evolution of CMIP6 SSP2-4.5 and SSP5-8.5 temperature anomalies
378 with respect to the baseline climate period (a). Comparison of CMIP6 SSP2-4.5 and
379 SSP5-8.5 temperature anomalies with respect to the baseline climate period for 2050-
380 2060 and 2090-2100 temporal periods (b). Figure 7 (c) and (d) are the same as Figure 7



381 (a) and (b), respectively, but for precipitation. The dots of (b) and (d) represent the
382 average of each CMIP6 model for the temporal period and climate variable.

383 We further assessed whether the temperature conditions reconstructed from ice-core data
384 are consistent with CRE dates from moraine boulders and can accurately replicate the
385 MIE of the Late Holocene. The IGM was spin-up and forced with the lowest error
386 configuration. Subsequently, a sensitivity analysis of temperature and precipitation was
387 conducted. The IGM was run after present-day steady-state conditions, with variations of
388 temperature from 0 to -1 by steps of 0.25°C. Precipitation was increased by 10%. We
389 determined the temperature and precipitation conditions that allowed the MIE of the Late
390 Holocene glacier extension, enabling its reconstruction (Figure 8).



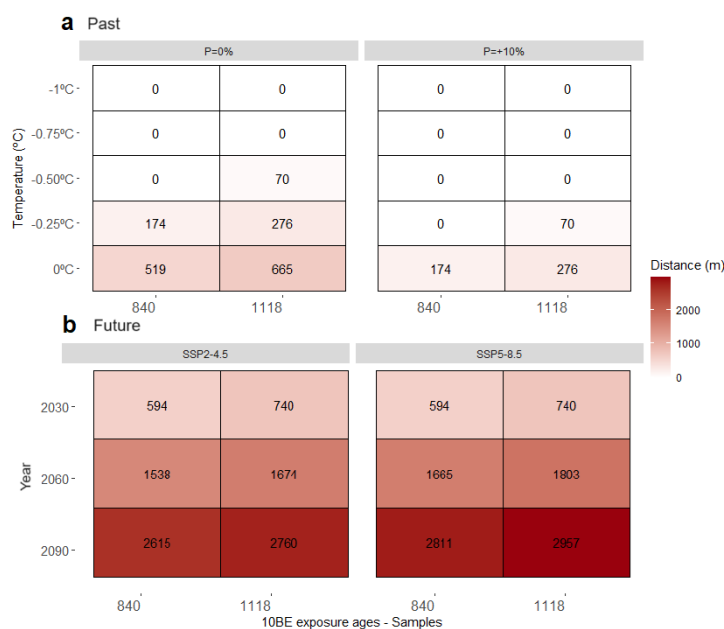
391

392 **Figure 8.** Location of the CRE samples (red dots) and average ice thickness (m) for
393 various temperature (T) and precipitation (P) perturbations. The ice thickness values
394 shown are the result of performing a spin-up model run, and subsequently a 1000-year
395 model run for reconstructing the MIE of the Late Holocene.

396 The assessment of past temperature and precipitation anomalies relative to the baseline
397 climate is conducted based on the distance between the glacier tongue and available CRE
398 dates. This analysis indicates the temperature and precipitation conditions that facilitated
399 glacier expansion during the MIE of the Late Holocene. Note that there may be a time
400 gap between MIE of the Late Holocene the timing of maximum ice expansion and CRE
401 ages and the since these ages indicate not the period of glacial growth but rather the period
402 when moraine boulders stabilized after the formation of the moraine ridges formed by the
403 glacier advances/stillstands. The minimum distance for all samples is reached when
404 temperature is reduced by 0.5°C and precipitation is increased by 10% with respect to the
405 baseline climate. A reduction of 0.75°C while maintaining precipitation unchanged
406 resulted in glacier advances to the limit marked by the dated moraine boulders (Figure 8
407 and 9). These findings suggest that temperature anomalies leading to glacier extension up



408 to the MIE of the Late Holocene ranged at least from temperatures of -0.5°C and
 409 precipitation of $+10\%$ to temperatures of $\leq -0.75^{\circ}\text{C}$ and precipitation of 0% relative to
 410 the baseline climate (Figure 9). However, a variation in precipitation of 10% is unlikely
 411 according to paleoclimate reconstructions for the Late Holocene (Badgley et al., 2020).
 412 This suggests that a temperature decrease of at least 0.75°C from the baseline climate,
 413 with no changes in precipitation, is the most plausible climate scenario.
 414



415

416 **Figure 9.** Differences in pixel distance (m) between the nearest modelled glacier
 417 extension and the sample age location (x-axis) across various air temperature (y-axis) and
 418 precipitation options (boxes) (a). Differences in pixel distance (m) between the nearest
 419 modelled glacier extension and the sample age location (x-axis) and projected glacier
 420 shrinkage for CMIP6 scenarios (boxes) and different years (y-axis).

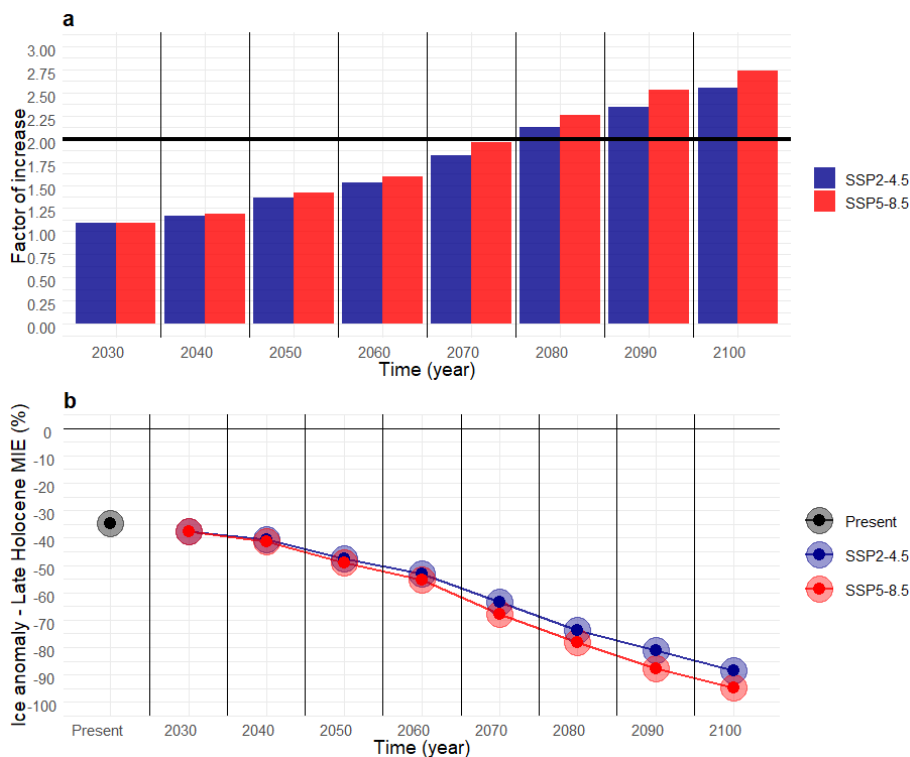
421 The results suggest that with -0.75°C and no changes in precipitation anomalies with
 422 respect to baseline climate, the glacier ice thickness has reduced 34% with respect to
 423 surface covered by glaciers during the MIE of the Late Holocene (Figure 10).

424 5.3 Future glacier changes

425 Assuming the PDD parametrization of the 2000–2020 period calibrated with geodetic data
 426 (Hugonnet et al., 2021), the future climate for 2060 leads to glacier tongue recession
 427 ranging from 1674 m (SSP2-4.5) to 1903 m (SSP5-8.5) relative to the MIE of the Late
 428 Holocene (Figures 9 to 11). By 2090, glacier reduction is projected to reach up to 2760 m
 429 (SSP2-4.5) or 2957 m (SSP5-8.5). These results indicate that the projected increase in
 430 precipitation (Figure 7) is insufficient to offset glacier shrinkage. The rate of ice loss from



431 the MIE of the Late Holocene to the present (34%) will double after 2070 (Figure 10a),
 432 regardless of the CMIP6 scenario. The rate of ice loss will increase by 2080, reaching
 433 anomalies of 72% (SSP2-4.5) and 78% (SSP5-8.5). By 2100 and under SSP5-8.5, the
 434 reduction in ice thickness will reach a maximum ice loss of 95% relative to the MIE of
 435 the Late Holocene (Figures 10b and 11).

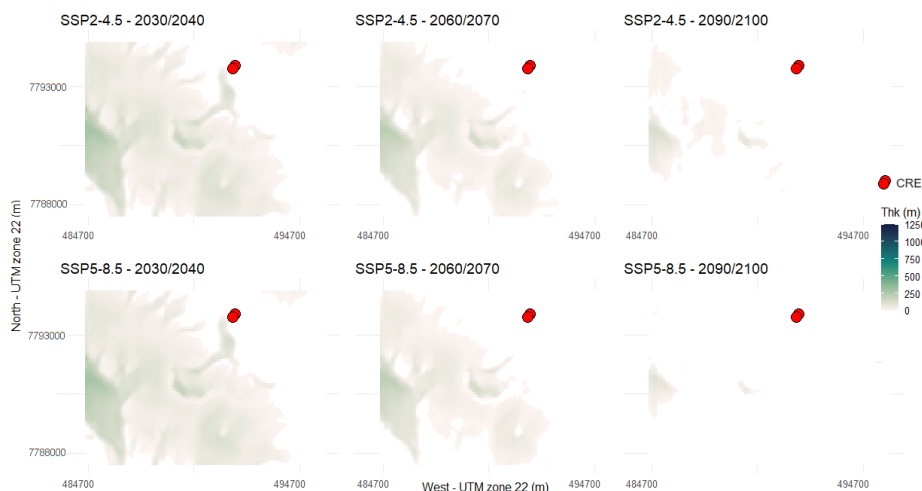


436

437 **Figure 10.** Factor of increase in ice loss under future climate change compared to ice loss
 438 from the MIE of the Late Holocene to the present (a). Ice thickness anomalies for the
 439 present and future CMIP6 SSP2-4.5 and SSP5-8.5 scenarios (b). Anomalies are calculated
 440 by subtracting the accumulated yearly ice thickness for the MIE of the Late Holocene (i)
 441 from the accumulated yearly ice thickness from the present-day (ii) and future ice-loss
 442 changes (iii), dividing by (i), and multiplying by 100. The factor of increase under future
 443 climate change is calculated by dividing future ice loss anomalies by the present-day ice
 444 loss anomalies relative to the MIE of the Late Holocene.

445

446



447

448 **Figure 11.** Location of the CRE samples (red dots) and average ice thickness (m) for
 449 future CMIP6 SSP2-4.5 and SSP5-8.5 scenarios and different temporal periods. The ice
 450 thickness values shown are the result of performing a spin-up model run reaching steady
 451 state conditions, and subsequently performing a model run with CMIP6 projections from
 452 present-day to 2100.

453 6. Discussion

454 6.1 Glacier modelling as a tool to understand paleoclimate conditions

455 The range of temperature decrease (0.75°C to 1°C) that obtained the best results in terms
 456 of reproducing glacier's MIE of Late Holocene area is consistent with past temperature
 457 anomalies in the Western and Southern Greenland found in previous works. Particularly,
 458 this range of temperature anomalies fall between estimates of ~1.5 °C cooler temperature
 459 at 1850 CE with respect to 1990s (Dahl-Jensen et al., 1998). In Southern-Western
 460 Greenland, temperature estimates derived from geospatial reconstruction of ELAs that
 461 attributed historical MIE to the LIA, suggest temperatures ranging from around -0.4 to -
 462 0.9 °C (Larocca et al., 2020). Employing a similar methodology, other studies have found
 463 temperature anomalies during the LIA to be of -1.1 ± 0.6 °C, with no observed changes
 464 in precipitation (Brooks et al., 2022).

465 However, the MIE of the Late Holocene in Central-Western Greenland defined by the
 466 most recent moraine complexes suggest an earlier maximum glacier extent than in other
 467 areas in the Northern Hemisphere when the LIA glacier expansion was much more
 468 extensive (Young et al., 2015). In this sense, the temperature indicated by at Northern-
 469 Hemispheric scale reanalysis for the MWP is not consistent with MIE obtained from
 470 glacier moraines dated with CRE in Western Greenland (Jomelli et al., 2016; Biette et al.,
 471 2019). Indeed, Biette et al. (2019) modelled the outlet glacier of the Lyngmarksbræen ice
 472 cap (Disko Island) and tested its sensitivity to temperature and precipitation using a PDD
 473 approach guided by temperature anomalies from a lake sediment located 250 km south of



474 Disko Island (D'Andrea et al., 2011). They demonstrated that the MIE of the Late
475 Holocene during the late MWP (1200 ± 130 CE) occurred when temperatures ranged
476 from -1.3°C to -1.6°C , and precipitation changed by $\pm 10\%$ (Biette et al., 2019).
477 Considering that the baseline climate period of our work is 1960 to 1990, and their
478 anomalies are considered to the end-20th century, our results are similar to these reported
479 temperature and precipitation values. These results are in line with a decrease in summer
480 temperature from -0.5° to -3°C at around 250 km of Disko Island during the MWP
481 obtained from lacustrine (alkenone-based lake sediment) reconstructions, and a second
482 cold phase during the LIA (D'Andrea et al., 2011). These cold conditions have been linked
483 to multi-decadal cold spells intense enough to cause a major advance of Baffin Bay during
484 the MWP (Young et al., 2015; Jomelli et al., 2016). These glacier advances were also
485 observed in other Northern Hemisphere glaciers and may be also enhanced by volcanic
486 eruptions (Solomina et al., 2016). The reconstructed glacier advances were probably
487 linked with a recurrent positive NAO at West Greenland and Baffin Bay during MWP
488 that lead to cool conditions (Young et al., 2015). However, other studies suggested that
489 the NAO was not predominantly positive during this period (Lasher and Axford, 2019).
490 There are also studies suggesting cold sea-surface temperatures observed during the
491 MWP (Sha et al., 2017), while others suggest warmer conditions during the MWP
492 compared to the LIA (Perner et al., 2012).

493 The MIE of the glaciers in the study area was reached during the MWP (1130 ± 40 and
494 925 ± 80 CE) (Young et al., 2015), has been suggested to be linked to increased snowfall
495 rates that counterbalanced the glacier ablation mass losses during the MWP, which were
496 slightly higher than those during the LIA (Osman et al., 2021). However, an increase of
497 precipitation of $+ 10\%$ with respect to the baseline climate period is not able to
498 counterbalance glacier recession under a change of $<-0.5^{\circ}\text{C}$ with respect to the baseline
499 climate (Figure 9). The sensitivity analysis performed here reveals that the glaciers were
500 far isothermal conditions within 1960-1990 period and a small decadal variation of
501 temperature with respect to the baseline analysis to temperature and precipitation
502 performed in this work is consistent with previous works that suggest that around 90% of
503 variation and that glacier maximum extension dynamics are linked with summer
504 temperature (Miller et al., 2012; Young et al., 2015).

505 **6.2 Central-Western Greenland ice-loss and comparison with other Greenland areas**

506 The reconstructed MIE of the Late Holocene represents the phase with most recent
507 widespread glacier advances from the Nuussuaq Peninsula, and it occurred prior to the
508 LIA (Schweinsberg et al., 2017; 2019). The maximum glacier advance reconstructed in
509 this work for Central-Western Greenland is not consistent across Greenland. Northern
510 GrIS exhibits stability during the Late Holocene with advances at 2.8 ka and 1650 CE
511 (Reusche et al., 2018). In particular, North-Western glaciers length was similar from 5.8
512 ka until onset of LIA (Søndergaard et al., 2020). In the Bregne Ice Cap (East Greenland)
513 glacier length dating reveals a peak during the LIA (~ 0.74 ka; Levy et al., 2014).
514 However, in Renland Ice Cap (Eastern Greenland) glacier exceeded present limits at 3.3



515 ka and around 1 ka, which is similar to LIA glacier advance (Medford et al., 2021). In
516 Central-East Greenland, cold climate conditions occurred during LIA at Stauning Alper
517 with peaks of 0.78 ± 0.31 ka (Kelly et al., 2008), and at Istorvet ice cap, that reached its
518 maximum Holocene extent at 0.8 ± 0.3 ka (Lowell et al., 2013). This expansion observed
519 in Eastern Greenland corresponds with peak glacier extensions seen in Iceland, attributed
520 to LIA (Flowers et al., 2008). Different asymmetries between Greenland sectors are seen
521 historically as revealed by long-term GICs recession larger in West Greenland than in
522 East, which has been attributed to the positive oscillation of NAO since the LIA that led
523 to warmer conditions in West Greenland due to the West-East NAO dipole (Björk et al.,
524 2018).

525 In Central-Western Greenland, most of the studies focusing on Late Holocene glacial
526 history come from near Disko Island (Ingolfsson et al., 1990; Humlum, 1998; Yde and
527 Knudsen, 2007; Citterio et al., 2009; Jomelli et al., 2016). Here, in its Eastern fringe, the
528 ELA from the LIA is estimated at ca. 550 ± 500 m, contrasting with values of 200-300 m
529 attributed elsewhere in the island (Ingolfsson et al., 1990). In the Western section,
530 however, the ELA during the LIA was estimated to be at 450 ± 420 m (Humlum, 1998).
531 As in Nuussuaq Peninsula, the Holocene maximum extension in Disko Island is
532 evidenced by moraine systems exhibiting a fresh, partly unvegetated appearance, with of
533 prevalence of *Rhizocarpon geographicum* in these moraines (Humlum, 1987). This
534 absence of Holocene moraine systems beyond the LIA moraines indicates that the
535 advance of LIA represents the maximum extension of this glacier since the Late Holocene
536 (Humlum, 1999). This moraine evidence has been used to estimate the ELA (Brooks et
537 al., 2022; Carrivick et al., 2023). Particularly, using geospatial methods Carrivick et al.
538 (2023) attributed this trimline to the maximum extent of LIA and concluded that
539 Greenland GICs lost 499 Gt since end-LIA, corresponding to 1.38 mm sea level
540 equivalent. Similarly, in Southern-Western Greenland, 42 GICs lost 48% of their area
541 since the LIA with respect to 2019 (Brooks et al., 2022). These values are slightly higher
542 than the 34 % reduction from the MIE of the Late Holocene with respect to present-day
543 glacier reported in this work. The differences could be attributed to the local relief
544 configuration as well as to the north aspect of the reconstructed glacier area and
545 methodological variances. Additionally, while we are employing a glacier modelling
546 approach constrained by geological records of a specific age, previous studies have
547 estimated distances based on ELAs and geospatial methods that account for spatial
548 distances between present-day glaciers tongue and maximum historical moraines that
549 could be formed prior to the LIA. According to remote sensing data, in Disko Island GICs
550 inventory and monitoring from 1953 to 2005 indicates that the average recession during
551 this timeframe amounted to 11% of the glacier lengths recorded in 1953 (number of
552 glaciers, $n = 172$), and 38% of the distance between LIA moraines and glacier termini in
553 1953 ($n = 87$) (Yde and Knudsen, 2007). These values are lower than those observed at
554 Pjetursson Glacier (Disko Island), which has retreated since the LIA with a decrease in
555 total glacier area of around 40% by the end of the 20th century according to geospatial
556 methods (Bøcker, 1996). Using remote sensing data, LIA to 2001 glacier shrinkage in



557 Central-Western Greenland was estimated in a reduction of ~ 20% of the area (Citterio et
558 al., 2009).

559 Currently, the modeled glacier area and volume are out of balance with respect to the
560 temperature since 1990 to present (figure not shown), necessitating the simulation of
561 glaciers using temperature and precipitation data from the 1960-1990 period (Figure 2).
562 This indicates a committed ice loss regardless of future climate scenarios. Future
563 projections show a remarkable increase in temperature, reaching HWP anomalies by 2050
564 and tripling HWP anomalies by 2100 under SSP5-8.5. Our results indicate that glacier
565 mass loss by >2070 will double the ice loss from the MIE of the Late Holocene to the
566 present. Precipitation is projected to increase by 20% (2050; SSP2-4.5 and SSP5-8.5) up
567 to 38% (2100; SSP5-8.5) compared to the baseline climate but cannot counterbalance
568 glacier losses. The modeled GICs mass loss is expected to reach MIE of the Late
569 Holocene anomalies of 95% by 2100 under SSP5-8.5. The data presented in this work
570 suggests that future glacier ice loss will occur at unprecedented rates compared to the
571 period from the MIE of the Late Holocene to the present.

572 Currently, the modeled glacier area and volume are out of balance with respect to the
573 temperature since 1990 to present (figure not shown), necessitating the simulation of
574 glaciers using temperature and precipitation data from the 1960-1990 period (Figure 2).
575 This indicates a committed ice loss regardless of future climate scenarios. Future
576 projections show a remarkable increase in temperature, reaching HWP anomalies by 2050
577 and tripling HWP anomalies by 2100 under SSP5-8.5. Our results indicate that glacier
578 mass loss by >2070 will double the ice loss from the MIE of the Late Holocene to the
579 present. Precipitation is projected to increase by 20% (2050; SSP2-4.5 and SSP5-8.5) up
580 to 38% (2100; SSP5-8.5) compared to the baseline climate but cannot counterbalance
581 glacier losses. The modeled GICs mass loss is expected to reach MIE of the Late
582 Holocene anomalies of 95% by 2100 under SSP5-8.5. The data presented in this work
583 suggests that future glacier ice loss will occur at unprecedented rates compared to the
584 period from the MIE of the Late Holocene to the present.

585 According to CMIP6 projections for near-ice-free zones of Disko Island, this temperature
586 increase is explained by increases in long-wave radiation and slight variations or
587 decreases in short-wave radiation (Bonsoms et al., 2024). Future winter temperatures are
588 expected to remain below isothermal conditions, leading to more snowfall during winter
589 (i.e., +22% for SSP5-8.5 for the 2090-2100 period, relative to the baseline climate). The
590 increase of snowfall, however, cannot counterbalance glacier shrinkage, and a 10%
591 increase in precipitation has minimal impact on glacier area and thickness variability
592 (Figure 8). Snowpack projections for a near-ice-free region of Disko Island align with
593 these findings, indicating decreases in snow depth and snowfall fraction, along with
594 increases in snow ablation (Bonsoms et al., 2024a). For the GrIS, previous studies
595 projected a larger SMB decrease in ice sheet margins due to higher melting and lower
596 accumulation compared to the GrIS interior; pointing out that increases in snowfall are
597 insufficient to counterbalance the increased runoff (Fettweis et al., 2013). Yet, CMIP6



598 models are unable to capture the increase in anticyclonic events in Greenland since 1990s
599 (Delhasse et al., 2021), which have driven increased melting and extreme melting events
600 in the GrIS (Bonsoms et al., 2024).

601 Greenland GICs numerical modelling reconstructions are scarce in comparison with GrIS
602 numerical modelling works; including paleoclimate modelling (Huybrechts, 2002),
603 model parameters sensitivity studies (Cuzzone et al., 2019) or GrIS Holocene evolution
604 constrained with geological records (i.e., Simpson et al., 2009; Lecavalier et al., 2014,
605 Briner et al., 2020). GICs make a modest (11 %) contribution to total Greenland ice loss
606 but exhibit a fast response to warming (Khan et al., 2019). While we modeled the response
607 of glaciers in a Central-Western GIC area, future studies should compare these ice loss
608 rates with GrIS trends, which exhibit a slower response to warming (Ingolfsson et al.,
609 1990). The anticipated glacier retreat has important environmental implications,
610 including increased freshwater release into the North Atlantic and alterations in
611 atmospheric and circulation patterns (Yu and Zhong, 2018), which may impact the
612 Atlantic Meridional Overturning Circulation (Thornalley et al., 2018). Thus, Greenland
613 glacial retreat, snow melting, and permafrost thaw will amplify greenhouse gases release
614 and potentially trigger major consequences at global scale (Miner et al., 2022). Negative
615 mass balances will change geomorphological and permafrost patterns (Christiansen et al.,
616 2010) and ecosystem dynamics in ice-free zones, by modifying maritime (Saros et al.,
617 2019), and terrestrial phenological and fauna distribution (John Anderson et al., 2017).

618 **6.3 Atmospheric forcing and numerical modelling considerations**

619 This work is based on GSWP3 W5E5v2.0 climate dataset, which is based on ERA5
620 reanalysis data bias-adjusted over land (Lange et al., 2021). ERA5 incorporates
621 observations via a data-assimilation system combining observations, modelling, and
622 satellite data, and was previously validated in Greenland (Delhasse et al., 2020). ERA5
623 has been used to force state-of-the-art regional climate models, showing good agreement
624 with observations (Box et al., 2022). Our results are consistent with previous works that
625 provided a glacier reconstruction based on outputs of MAR forced with ERA5 and a PDD
626 model in Disko Island (Central-Western Greenland) (Biette et al., 2019). Results are
627 indeed similar to geo-spatial reconstructions in other Greenland sectors (i.e., Brooks et
628 al., 2022). The main conclusions of this work are consistent with paleo GrIS
629 reconstructions and projections in Central-Western GrIS (Briner et al. 2020).

630 A more sophisticated glacier modelling experiment will require data from coupling
631 regional circulation models, which account for changes in large-scale circulation.
632 However, glacier modelling driven by paleoclimate simulations has uncertainties and
633 large variability between models, as previous works in the study area have shown that
634 paleoclimate simulations cannot reconstruct Late Holocene glacier dynamics in the study
635 area (Jomelli et al., 2016; Biette et al., 2019). Paleoglacier modelling forced with
636 convection-permitting models is computationally demanding, relies on
637 parameterizations, and has limitations in simulating paleoclimate variables (Russo et al.,
638 2024). In this work a sensitivity analysis to precipitation and temperature is conducted to



639 reconstruct glacier MIE based on cosmogenic data, and therefore results are analyzed
640 based on anomalies with respect to a baseline climate (1960-1990), which is sufficiently
641 long to consider climate interannual variability and is marginally affected by climate
642 warming.

643 As with most paleo glacier models, IGM relies on a PDD approach, which is an
644 approximation that does not account for the Surface Energy Balance (SEB) driving
645 melting. However, the SEB components required for glacier modelling are uncertain for
646 the spatial and temporal scales analyzed in this study. PDD is based on a temperature
647 index model. Impurities on the ice (such as algae, dust, etc.) are not directly considered
648 but indirectly inferred by the melt rate factor. The IGM configuration for the calibration
649 and correction process of precipitation and temperature is based on OGGM v1.6.1
650 (Maussion et al., 2015; Schuster et al., 2023). This calibration corrects precipitation and
651 temperature to match geodetic mass balance at the glacier level (Hugonnet et al., 2021).
652 This product was selected due to the lack of long-term past and present in-situ mass
653 balance measurements in the study area. Errors of Hugonnet et al. (2021) product are
654 therefore influencing the glacier modelling results. The OGGM v1.6.1 calibration of bias
655 correction has been recently compared and cross-validated for glacier modelling of past
656 and future glacier projections, demonstrating reliable results (i.e., Aguayo et al., 2023;
657 Zekollari et al., 2024, and references therein).

658 IGM has been previously validated for modelling the present and projecting the future
659 evolution of glaciers, being successfully applied to the present and future scenarios of
660 alpine glaciers and providing reliable results (Cook et al., 2023); and references therein).
661 Here we have performed a IGM parameter tuning to accurately simulate present-day
662 glacier conditions. We cross validated results against two independent ice thickness
663 products (Farinotti et al., 2019; Millan et al., 2022) and RGI6.0 observations. Data shows
664 good agreement when compared to Farinotti et al. (2019) but lesser agreement against
665 Millan et al. (2022) (Figure 4). These differences could be attributed to the different
666 glacier methodologies: Farinotti et al. (2019) is based on an ensemble of five glacier
667 models founded on ice flow physics, whereas Millan et al. (2022) is based on glacier flow
668 mapping. Further research should analyze these differences. As most numerical modelling
669 experiments, past and future ice flow parameters are likely different from present-day
670 parameters due to unknown variables such as variations in basal conditions, bedrock
671 topography, and ice rheology. Consequently, IGM parametrization should be seen as a
672 simplification when applied to past and future conditions due to the difficulty of inferring
673 these parameters accurately.

674

675 **7. Conclusions**

676 This work analyzes the long-term dynamics of Central-Western GICs Greenland's and
677 their response to climate variability. We integrated ancillary data, ice thickness estimates



678 and geological records to increase the understanding of paleoclimate conditions in this
679 zone and contextualize present and future glacier loss within the Holocene.

680 The IGM underwent calibration and validation with various parametrization options of A
681 and c to accurately replicate glacier ice thickness and area. Following a long-term spin-
682 up simulation, the model converged to stable glacier conditions, matching available ice
683 thickness data and RGI6.0 area obtained from satellite observations and glacier
684 modelling. The optimal configuration reproduced available ice-thickness estimates,
685 representing an error of $<10\%$ of the total accumulated ice thickness for the modelled
686 area. Subsequently, the model was forced with an ensemble of temperature and
687 precipitation options, which were validated with CRE records, allowing to quantify
688 current glacier retreat since MIE of the Late Holocene. Further, IGM was forced with
689 CMIP6 projections towards 2100, allowing us to compare past and future recession within
690 a changing climate.

691 Results show that past glacier extensions during the MIE of the Late Holocene were
692 reached with temperature reductions that were likely to be between -0.75°C to -1°C with
693 respect to the baseline (1960-1990) climate period. Present-day reductions in glacier area
694 are 34% with respect to MIE of the Late Holocene. Results demonstrate the current
695 imbalance of Central-Western GICs and quantify how unprecedented are glacier shrinkage
696 within the Late Holocene. Future climate change will double the ice loss from Late
697 Holocene to present by > 2070 . By 2100 and under SSP5-8.5, glacier mass is projected
698 to be reduced 95 % with respect to the MIE of the Late Holocene, with implications for
699 regional hydrology, ecosystems, and sea-level rise. The results provide a better
700 understanding of the response of Arctic peripheral glaciers and ice caps to climate change,
701 anticipating the formation of new landscapes, deglaciated areas, and lakes.

702

703 **Code and data availability**

704 IGM is an open-access model provided at <https://github.com/jouvetg/igm> (Jouvet, 2023).

705 Data of this work are available upon request to the first author (josepbonsoms5@ub.edu).

706 **Author contributions**

707 JB, MO and JILM conceptualized and designed the work. JB wrote the manuscript. JB,
708 MO and JILM edited the manuscript and contributed to the discussion of the results. JB
709 led the modelling of the work guided by GJ. GJ provided comments on the modelling
710 aspects of the manuscript. MO and JILM supervised the project and acquired funding.

711 **Competing interests**

712 The authors have not competing interests.

713 **Acknowledgements**

714 This manuscript falls within the research topics examined by the research group Antarctic,
715 Arctic and Alpine Environments (ANTALP; 2017-SGR-1102) funded by the Government
716 of Catalonia and MARGISNOW (PID2021-124220OB-100), from the Spanish Ministry
717 of Science, Innovation and Universities. Josep Bonsoms is supported by a pre-doctoral



718 FPI grant (PRE2021097046) funded by the Spanish Ministry of Science, Innovation and
719 Universities.

720 **8. References**

721 Aguayo, R., Maussion, F., Schuster, L., Schaefer, M., Caro, A., Schmitt, P., Mackay, J.,
722 Ultee, L., Leon-Muñoz, J., and Aguayo, M.: Assessing the glacier projection uncertainties
723 in the Patagonian Andes (40-56° S) from a catchment perspective,
724 <https://doi.org/10.5194/egusphere-2023-2325>, 2024.

725 Badgeley, J. A., Steig, E. J., Hakim, G. J., and Fudge, T. J.: Greenland temperature and
726 precipitation over the last 20000 years using data assimilation, *Climate of the Past*, 16,
727 1325–1346, <https://doi.org/10.5194/cp-16-1325-2020>, 2020.

728 Biette, M., Jomelli, V., Favier, V., Chenet, M., Agosta, C., Fettweis, X., Minh, D.H.T.,
729 Ose, K., 2018. Estimation des températures au début du dernier millénaire dans l'ouest
730 du Groenland : résultats préliminaires issus de l'application d'un modèle glaciologique
731 de type degré jour sur le glacier du Lyngmarksbræen. *Géomorphologie Relief Process.*
732 *Environ.* 24. <https://doi.org/10.4000/geomorphologie.11977>

733 Bjørk, A. A., Aagaard, S., Lütt, A., Khan, S. A., Box, J. E., Kjeldsen, K. K., Larsen, N.
734 K., Korsgaard, N. J., Cappelen, J., Colgan, W. T., Machguth, H., Andresen, C. S., Peings,
735 Y., and Kjær, K. H.: Changes in Greenland's peripheral glaciers linked to the North
736 Atlantic Oscillation, *Nat Clim Chang*, 8, 48–52, [https://doi.org/10.1038/s41558-017-](https://doi.org/10.1038/s41558-017-0029-1)
737 0029-1, 2018.

738 Bøcker, C. A.: Using GIS for glacier volume calculations and topographic influence of
739 the radiation balance. An example from Disko, West Greenland, *Geografisk Tidsskrift*,
740 11–20, <https://doi.org/10.1080/00167223.1996.10649372>, 1996.

741 Bolch, T., Sandberg Sørensen, L., Simonsen, S. B., Mölg, N., MacHguth, H., Rastner, P.,
742 and Paul, F.: Mass loss of Greenland's glaciers and ice caps 2003-2008 revealed from
743 ICESat laser altimetry data, *Geophys Res Lett*, 40, 875–881,
744 <https://doi.org/10.1002/grl.50270>, 2013.

745 Bonsoms, J., Oliva, M., Alonso-González, E., Revuelto, J., and López-Moreno, J. I.:
746 Impact of climate change on snowpack dynamics in coastal Central-Western Greenland,
747 *Science of the Total Environment*, 913, <https://doi.org/10.1016/j.scitotenv.2023.169616>,
748 2024a.

749 Bonsoms, J., Oliva, M., López-Moreno, J. I. and Fettweis, X. Rising extreme meltwater
750 trends in Greenland ice sheet (1950 – 2022): surface energy balance and large-scale
751 circulation changes. *J. Climate*, <https://doi.org/10.1175/JCLI-D-23-0396.1>, in press,
752 2024b.

753 Briner, J. P., Cuzzzone, J. K., Badgeley, J. A., Young, N. E., Steig, E. J., Morlighem, M.,
754 Schlegel, N. J., Hakim, G. J., Schaefer, J. M., Johnson, J. V., Lesnek, A. J., Thomas, E.
755 K., Allan, E., Bennike, O., Cluett, A. A., Csatho, B., de Vernal, A., Downs, J., Larour, E.,



- 756 and Nowicki, S.: Rate of mass loss from the Greenland Ice Sheet will exceed Holocene
757 values this century, *Nature*, 586, 70–74, <https://doi.org/10.1038/s41586-020-2742-6>,
758 2020.
- 759 Brooks, J. P., Larocca, L. J., and Axford: Little Ice Age climate in southernmost Greenland
760 inferred from 1 quantitative geospatial analyses of alpine glacier reconstructions, 2022.
- 761 Buizert, C., Keisling, B. A., Box, J. E., He, F., Carlson, A. E., Sinclair, G., and DeConto,
762 R. M.: Greenland-Wide Seasonal Temperatures During the Last Deglaciation, *Geophys*
763 *Res Lett*, 45, 1905–1914, <https://doi.org/10.1002/2017GL075601>, 2018.
- 764 Cappelen, J.: Weather and climate data from Greenland 1958-2011-Observation data with
765 description, n.d.
- 766 Carrivick, J. L., Boston, C. M., Sutherland, J. L., Pearce, D., Armstrong, H., Bjørk, A.,
767 Kjeldsen, K. K., Abermann, J., Oien, R. P., Grimes, M., James, W. H. M., and Smith, M.
768 W.: Mass Loss of Glaciers and Ice Caps Across Greenland Since the Little Ice Age,
769 *Geophys Res Lett*, 50, <https://doi.org/10.1029/2023GL103950>, 2023.
- 770 Christiansen, H. H., Etzelmüller, B., Isaksen, K., Juliussen, H., Farbrøt, H., Humlum, O.,
771 Johansson, M., Ingeman-Nielsen, T., Kristensen, L., Hjort, J., Holmlund, P., Sannel, A.
772 B. K., Sigsgaard, C., Åkerman, H. J., Foged, N., Blikra, L. H., Pernosky, M. A., and
773 Ødegård, R. S.: The thermal state of permafrost in the nordic area during the international
774 polar year 2007-2009, *Permafrost Periglacial Process*, 21, 156–181,
775 <https://doi.org/10.1002/ppp.687>, 2010.
- 776 Citterio, M., Paul, F., Ahlstrøm, A. P., Jepsen, H. F., and Weidick, A.: Remote sensing of
777 glacier change in West Greenland: Accounting for the occurrence of surge-type glaciers,
778 *Ann Glaciol*, 50, 70–80, <https://doi.org/10.3189/172756410790595813>, 2009.
- 779 Cronauer, S. L., Briner, J. P., Kelley, S. E., Zimmerman, S. R. H., and Morlighem, M.:
780 ¹⁰Be dating reveals early-middle Holocene age of the Drygalski Moraines in central West
781 Greenland, *Quat Sci Rev*, 147, 59–68, <https://doi.org/10.1016/j.quascirev.2015.08.034>,
782 2016.
- 783 Cucchi, M., P. Weedon, G., Amici, A., Bellouin, N., Lange, S., Müller Schmied, H.,
784 Hersbach, H., and Buontempo, C.: WFDE5: Bias-adjusted ERA5 reanalysis data for
785 impact studies, *Earth Syst Sci Data*, 12, 2097–2120, <https://doi.org/10.5194/essd-12-2097-2020>, 2020.
- 787 Cuzzone, J. K., Schlegel, N. J., Morlighem, M., Larour, E., Briner, J. P., Seroussi, H., and
788 Caron, L.: The impact of model resolution on the simulated Holocene retreat of the
789 southwestern Greenland ice sheet using the Ice Sheet System Model (ISSM), *Cryosphere*,
790 13, 879–893, <https://doi.org/10.5194/tc-13-879-2019>, 2019.
- 791 Cook, S. J., Jouvét, G., Millan, R., Rabatel, A., Zekollari, H., and Dussailant, I.:
792 Committed Ice Loss in the European Alps Until 2050 Using a Deep-Learning-Aided 3D



- 793 Ice-Flow Model With Data Assimilation, *Geophys Res Lett*, 50,
794 <https://doi.org/10.1029/2023GL105029>, 2023.
- 795 D'andrea, W. J., Huang, Y., Fritz, S. C., and Anderson, N. J.: Abrupt Holocene climate
796 change as an important factor for human migration in West Greenland,
797 <https://doi.org/10.1073/pnas.1101708108/-/DCSupplemental>, 2011.
- 798 Farinotti, D., Huss, M., Fürst, J.J. et al. A consensus estimate for the ice thickness
799 distribution of all glaciers on Earth. *Nat. Geosci.* 12, 168–173,
800 <https://doi.org/10.1038/s41561-019-0300-3>, 2019.
- 801 Flowers, G. E., Björnsson, H., Geirsdóttir, Á., Miller, G. H., Black, J. L., and Clarke, G.
802 K. C.: Holocene climate conditions and glacier variation in central Iceland from physical
803 modelling and empirical evidence, *Quat Sci Rev*, 27, 797–813,
804 <https://doi.org/10.1016/j.quascirev.2007.12.004>, 2008.
- 805 Glen, J. W. The Creep of Polycrystalline Ice, *Proceedings of the Royal Society of London.*
806 *Series A, Mathematical and Physical Sciences* (1934-1990), 228(1175), 519538,
807 doi:10.1098/rspa.1955.0066, 1955.
- 808 Hanna, E., Mernild, S. H., Cappelen, J., and Steffen, K.: Recent warming in Greenland in
809 a long-term instrumental (1881-2012) climatic context: I. Evaluation of surface air
810 temperature records, *Environmental Research Letters*, 7, <https://doi.org/10.1088/1748-9326/7/4/045404>, 2012.
- 812 Hansen, B. U., Elberling, B., Humlum, O., and Nielsen, N.: Meteorological trends (1991-
813 2004) at Arctic Station, Central West Greenland (69°15'N) in a 130 years perspective,
814 *Geografisk Tidsskrift*, 106, 45–55, <https://doi.org/10.1080/00167223.2006.10649544>,
815 2006.
- 816 Helama, S., Jones, P. D., and Briffa, K. R. Dark Ages Cold Period: A literature review and
817 directions for future research. *The Holocene*, 27(10), 1600-1606.
818 <https://doi.org/10.1177/0959683617693898>, 2017.
- 819 Hock, R.: Temperature index melt modelling in mountain areas, *J Hydrol (Amst)*, 282,
820 104–115, [https://doi.org/10.1016/S0022-1694\(03\)00257-9](https://doi.org/10.1016/S0022-1694(03)00257-9), 2003.
- 821 Hugonnet, R., McNabb, R., Berthier, E., Menounos, B., Nuth, C., Girod, L., Farinotti, D.,
822 Huss, M., Dussaillant, I., Brun, F., and Kääb, A.: Accelerated global glacier mass loss in
823 the early twenty-first century, *Nature*, 592, 726–731, <https://doi.org/10.1038/s41586-021-03436-z>, 2021.
- 825 Humlum, O.: The climatic significance of rock glaciers, *Permafrost Periglacial Process*, 9, 375–
826 395, [https://doi.org/10.1002/\(SICI\)1099-1530\(199810/12\)9:4<375::AID-PPP301>3.0.CO;2-0](https://doi.org/10.1002/(SICI)1099-1530(199810/12)9:4<375::AID-PPP301>3.0.CO;2-0), 1998.
- 828 Humlum, O.: Late-Holocene climate in central West Greenland: meteorological data and
829 rock-glacier isotope evidence, *The Holocene*, 581–594 pp., 1999.



- 830 Huss, M., Bauder, A., Funk, M., and Hock, R.: Determination of the seasonal mass
831 balance of four Alpine glaciers since 1865, *J Geophys Res Earth Surf*, 113,
832 <https://doi.org/10.1029/2007JF000803>, 2008.
- 833 Ingolfsson, O., Frich, P., Funder, S., and Humlum O, O. B.: 12 01: Paleoclimatic
834 implications of an early Holocene glacier advance on Disko Island, West Greenland.
835 *Boreav*, 297–311 pp., 1990.
- 836 IPCC: High Mountain Areas, in: *The Ocean and Cryosphere in a Changing Climate*,
837 Cambridge University Press, 131–202, <https://doi.org/10.1017/9781009157964.004>,
838 2022.
- 839 Jiang, S., Ye, A., and Xiao, C.: The temperature increase in Greenland has accelerated in
840 the past five years, *Glob Planet Change*, 194,
841 <https://doi.org/10.1016/j.gloplacha.2020.103297>, 2020.
- 842 John Anderson, N., Saros, J. E., Bullard, J. E., Cahoon, S. M. P., McGowan, S., Bagshaw,
843 E. A., Barry, C. D., Bindler, R., Burpee, B. T., Carrivick, J. L., Fowler, R. A., Fox, A. D.,
844 Fritz, S. C., Giles, M. E., Hamerlik, L., Ingeman-Nielsen, T., Law, A. C., Mernild, S. H.,
845 Northington, R. M., Osburn, C. L., Pla-Rabès, S., Post, E., Telling, J., Stroud, D. A.,
846 Whiteford, E. J., Yallop, M. L., and Yde, A. J. C.: The arctic in the twenty-first century:
847 Changing biogeochemical linkages across a paraglacial landscape of Greenland,
848 <https://doi.org/10.1093/biosci/biw158>, 1 February 2017.
- 849 Jomelli, V., Lane, T., Favier, V., Masson-Delmotte, V., Swingedouw, D., Rinterknecht, V.,
850 Schimmelpfennig, I., Brunstein, D., Verfaillie, D., Adamson, K., Leanni, L., Mokadem,
851 F., Aumaître, G., Bourlès, D. L., and Keddadouche, K.: Paradoxical cold conditions
852 during the medieval climate anomaly in the Western Arctic, *Sci Rep*, 6,
853 <https://doi.org/10.1038/srep32984>, 2016.
- 854 Juvet, G.: Inversion of a Stokes glacier flow model emulated by deep learning, *Journal*
855 *of Glaciology*, 69, 13–26, <https://doi.org/10.1017/jog.2022.41>, 2023a.
- 856 Juvet, G., Cordonnier, G., Kim, B., Lüthi, M., Vieli, A., and Aschwanden, A.: Deep
857 learning speeds up ice flow modelling by several orders of magnitude, *Journal of*
858 *Glaciology*, 68, 651–664, <https://doi.org/10.1017/jog.2021.120>, 2022.
- 859 Juvet, G., Cohen, D., Russo, E., Buzan, J., Raible, C. C., Haeberli, W., Kamleitner, S.,
860 Ivy-Ochs, S., Imhof, M. A., Becker, J. K., Landgraf, A., and Fischer, U. H.: Coupled
861 climate-glacier modelling of the last glaciation in the Alps, *Journal of Glaciology*,
862 <https://doi.org/10.1017/jog.2023.74>, 2023c.
- 863 Kelley, S. E., Briner, J. P., and Young, N. E.: Rapid ice retreat in Disko Bugt supported
864 by ¹⁰Be dating of the last recession of the western Greenland Ice Sheet, *Quat Sci Rev*,
865 82, 13–22, <https://doi.org/10.1016/j.quascirev.2013.09.018>, 2013.



- 866 Kelly, M. A. and Lowell, T. V.: Fluctuations of local glaciers in Greenland during latest
867 Pleistocene and Holocene time, *Quat Sci Rev*, 28, 2088–2106,
868 <https://doi.org/10.1016/j.quascirev.2008.12.008>, 2009.
- 869 Kelly, M. A., Lowell, T. V., Hall, B. L., Schaefer, J. M., Finkel, R. C., Goehring, B. M.,
870 Alley, R. B., and Denton, G. H.: A ^{10}Be chronology of lateglacial and Holocene mountain
871 glaciation in the Scoresby Sund region, east Greenland: implications for seasonality
872 during lateglacial time, *Quat Sci Rev*, 27, 2273–2282,
873 <https://doi.org/10.1016/j.quascirev.2008.08.004>, 2008.
- 874 Khan, S. A., Colgan, W., Neumann, T. A., van den Broeke, M. R., Brunt, K. M., Noël, B.,
875 Bamber, J. L., Hassan, J., and Björk, A. A.: Accelerating Ice Loss From Peripheral
876 Glaciers in North Greenland, *Geophys Res Lett*, 49,
877 <https://doi.org/10.1029/2022GL098915>, 2022.
- 878 Kienholz, C., Rich, J. L., Arendt, A. A., and Hock, R.: A new method for deriving glacier
879 centerlines applied to glaciers in Alaska and northwest Canada, *Cryosphere*, 8, 503–519,
880 <https://doi.org/10.5194/tc-8-503-2014>, 2014.
- 881 Kingma, D. P. and Ba, J.: Adam: A Method for Stochastic Optimization, 2014.
- 882 Kjær, K. H., Björk, A. A., Kjeldsen, K. K., Hansen, E. S., Andresen, C. S., Siggaard-
883 Andersen, M. L., Khan, S. A., Søndergaard, A. S., Colgan, W., Schomacker, A.,
884 Woodroffe, S., Funder, S., Rouillard, A., Jensen, J. F., and Larsen, N. K.: Glacier response
885 to the Little Ice Age during the Neoglacial cooling in Greenland,
886 <https://doi.org/10.1016/j.earscirev.2022.103984>, 1 April 2022.
- 887 Lange, S., Menz, C., Gleixner, S., Cucchi, M., Weedon, G. P., Amici, A., Bellouin, N.,
888 Müller Schmied, H., Hersbach, H., Buontempo, C., and Cagnazzo, C.: WFDE5 over land
889 merged with ERA5 over the ocean (W5E5 v2.0), ISIMIP Repository [data set],
890 <https://doi.org/10.48364/ISIMIP.342217>, 2021.
- 891 Larocca, L. J., Axford, Y., Björk, A. A., Lasher, G. E., and Brooks, J. P.: Local glaciers
892 record delayed peak Holocene warmth in south Greenland, *Quat Sci Rev*, 241,
893 <https://doi.org/10.1016/j.quascirev.2020.106421>, 2020.
- 894 Larocca, L. J., Twining–Ward, M., Axford, Y., Schweinsberg, A. D., Larsen, S. H.,
895 Westergaard–Nielsen, A., Luetzenburg, G., Briner, J. P., Kjeldsen, K. K., and Björk, A.
896 A.: Greenland-wide accelerated retreat of peripheral glaciers in the twenty-first century,
897 *Nat Clim Chang*, 13, 1324–1328, <https://doi.org/10.1038/s41558-023-01855-6>, 2023.
- 898 Lasher, G. E. and Axford, Y.: Medieval warmth confirmed at the Norse Eastern Settlement
899 in Greenland, *Geology*, 47, 267–270, <https://doi.org/10.1130/G45833.1>, 2019.
- 900 Lecavalier, B. S., Milne, G. A., Simpson, M. J. R., Wake, L., Huybrechts, P., Tarasov, L.,
901 Kjeldsen, K. K., Funder, S., Long, A. J., Woodroffe, S., Dyke, A. S., and Larsen, N. K.: A
902 model of Greenland ice sheet deglaciation constrained by observations of relative sea



- 903 level and ice extent, *Quat Sci Rev*, 102, 54–84,
904 <https://doi.org/10.1016/j.quascirev.2014.07.018>, 2014.
- 905 Leclercq, P. W., Weidick, A., Paul, F., Bolch, T., Citterio, M., and Oerlemans, J.: Brief
906 communication historical glacier length changes in West Greenland, *Cryosphere*, 6,
907 1339–1343, <https://doi.org/10.5194/tc-6-1339-2012>, 2012.
- 908 Leger, T. P. M., Clark, C. D., Huynh, C., Jones, S., Ely, J. C., Bradley, S. L., Diemont, C.,
909 and Hughes, A. L. C.: A Greenland-wide empirical reconstruction of paleo ice sheet
910 retreat informed by ice extent markers: PaleoGrIS version 1.0, *Climate of the Past*, 20,
911 701–755, <https://doi.org/10.5194/cp-20-701-2024>, 2024.
- 912 Lowell, T. V., Hall, B. L., Kelly, M. A., Bennike, O., Lusas, A. R., Honsaker, W., Smith,
913 C. A., Levy, L. B., Travis, S., and Denton, G. H.: Late Holocene expansion of Istorvet ice
914 cap, Liverpool Land, east Greenland, *Quat Sci Rev*, 63, 128–140,
915 <https://doi.org/10.1016/j.quascirev.2012.11.012>, 2013.
- 916 Maussion, F., Butenko, A., Champollion, N., Dusch, M., Eis, J., Fourteau, K., Gregor, P.,
917 Jarosch, A. H., Landmann, J., Oesterle, F., Recinos, B., Rothenpieler, T., Vlug, A., Wild,
918 C. T., and Marzeion, B.: The Open Global Glacier Model (OGGM) v1.1, *Geosci. Model
919 Dev.*, 12, 909–931, <https://doi.org/10.5194/gmd12-909-2019>, 2019.
- 920 Medford, A. K., Hall, B. L., Lowell, T. V., Kelly, M. A., Levy, B., Wilcox, P. S., and
921 Axford, Y.: Holocene glacial history of Renland Ice Cap, East Greenland, reconstructed
922 from lake sediments, 2021.
- 923 Millan, R., Mouginot, J., Rabatel, A., and Morlighem, M.: Ice velocity and thickness of
924 the world’s glaciers, *Nat Geosci*, 15, 124–129, <https://doi.org/10.1038/s41561-021-00885-z>, 2022.
- 926 Miller, G. H., Geirsdóttir, Á., Zhong, Y., Larsen, D. J., Otto-Bliesner, B. L., Holland, M.
927 M., Bailey, D. A., Refsnider, K. A., Lehman, S. J., Southon, J. R., Anderson, C.,
928 Björnsson, H., and Thordarson, T.: Abrupt onset of the Little Ice Age triggered by
929 volcanism and sustained by sea-ice/ocean feedbacks, *Geophys Res Lett*, 39,
930 <https://doi.org/10.1029/2011GL050168>, 2012.
- 931 Miner, K. R., Turetsky, M. R., Malina, E., Bartsch, A., Tamminen, J., McGuire, A. D.,
932 Fix, A., Sweeney, C., Elder, C. D., and Miller, C. E.: Permafrost carbon emissions in a
933 changing Arctic, <https://doi.org/10.1038/s43017-021-00230-3>, 1 January 2022.
- 934 O’Hara, S. L., Briner, J. P., and Kelley, S. E.: A ^{10}Be chronology of early Holocene local
935 glacier moraines in central West Greenland, *Boreas*, 46, 655–666,
936 <https://doi.org/10.1111/bor.12234>, 2017.
- 937 Osman, M. B., Smith, B. E., Trusel, L. D., Das, S. B., McConnell, J. R., Chellman, N.,
938 Arienzo, M., and Sodemann, H.: Abrupt Common Era hydroclimate shifts drive west
939 Greenland ice cap change, *Nat Geosci*, 14, 756–761, <https://doi.org/10.1038/s41561-021-00818-w>, 2021.



- 941 Pedersen, A. K., Larsen, L. M., Riisager, P., and Dueholm, K. S.: Rates of volcanic
942 deposition, facies changes and movements in a dynamic basin: The Nuussuaq Basin, West
943 Greenland, around the C27n-C26r transition, *Geol Soc Spec Publ*, 197, 157–181,
944 <https://doi.org/10.1144/GSL.SP.2002.197.01.07>, 2002.
- 945 Reusche, M. M., Marcott, S. A., Ceperley, E. G., Barth, A. M., Brook, E. J., Mix, A. C.,
946 and Caffee, M. W.: Early to Late Holocene Surface Exposure Ages From Two Marine-
947 Terminating Outlet Glaciers in Northwest Greenland, *Geophys Res Lett*, 45, 7028–7039,
948 <https://doi.org/10.1029/2018GL078266>, 2018.
- 949 Rounce, D. R., Hock, R., Maussion, F., Hugonnet, R., Kochtitzky, W., Huss, M., Berthier,
950 E., Brinkerhoff, D., Compagno, L., Copland, L., Farinotti, D., Menounos, B., and
951 McNabb, R. W.: Global glacier change in the 21st century: Every increase in temperature
952 matters, *Science (80-.)*, 379, 78–83, <https://doi.org/10.1126/science.abo1324>, 2023.
- 953 Russo, E., Buzan, J., Lienert, S., Jouvét, G., Velasquez Alvarez, P., Davis, B., Ludwig, P.,
954 Joos, F., and Raible, C. C.: High-resolution LGM climate of Europe and the Alpine region
955 using the regional climate model WRF, *Clim. Past*, 20, 449–465,
956 <https://doi.org/10.5194/cp-20-449-2024>, 2024.
- 957 Saros, J. E., Anderson, N. J., Juggins, S., McGowan, S., Yde, J. C., Telling, J., Bullard, J.
958 E., Yallop, M. L., Heathcote, A. J., Burpee, B. T., Fowler, R. A., Barry, C. D., Northington,
959 R. M., Osburn, C. L., Pla-Rabes, S., Mernild, S. H., Whiteford, E. J., Grace Andrews, M.,
960 Kerby, J. T., and Post, E.: Arctic climate shifts drive rapid ecosystem responses across the
961 West Greenland landscape, *Environmental Research Letters*, 14,
962 <https://doi.org/10.1088/1748-9326/ab2928>, 2019.
- 963 Schweinsberg, A. D., Briner, J. P., Miller, G. H., Bennike, O., and Thomas, E. K.: Local
964 glaciation in West Greenland linked to North Atlantic ocean circulation during the
965 Holocene, *Geology*, 45, 195–198, <https://doi.org/10.1130/G38114.1>, 2017.
- 966 Schweinsberg, A. D., Briner, J. P., Licciardi, J. M., Bennike, O., Lifton, N. A., Graham,
967 B. L., Young, N. E., Schaefer, J. M., and Zimmerman, S. H.: Multiple independent records
968 of local glacier variability on Nuussuaq, West Greenland, during the Holocene, *Quat Sci
969 Rev*, 215, 253–271, <https://doi.org/10.1016/j.quascirev.2019.05.007>, 2019.
- 970 Simpson, M. J. R., Milne, G. A., Huybrechts, P., and Long, A. J.: Calibrating a
971 glaciological model of the Greenland ice sheet from the Last Glacial Maximum to
972 present-day using field observations of relative sea level and ice extent, *Quat Sci Rev*, 28,
973 1631–1657, <https://doi.org/10.1016/j.quascirev.2009.03.004>, 2009.
- 974 Solomina, O. N., Bradley, R. S., Jomelli, V., Geirsdottir, A., Kaufman, D. S., Koch, J.,
975 McKay, N. P., Masiokas, M., Miller, G., Nesje, A., Nicolussi, K., Owen, L. A., Putnam,
976 A. E., Wanner, H., Wiles, G., and Yang, B.: Glacier fluctuations during the past 2000
977 years, <https://doi.org/10.1016/j.quascirev.2016.04.008>, 1 October 2016.



- 978 Søndergaard, A. S., Larsen, N. K., Lecavalier, B. S., Olsen, J., Fitzpatrick, N. P., Kjær, K.
979 H., and Khan, S. A.: Early Holocene collapse of marine-based ice in northwest Greenland
980 triggered by atmospheric warming, *Quat Sci Rev*, 239,
981 <https://doi.org/10.1016/j.quascirev.2020.106360>, 2020.
- 982 Thornalley, D. J. R., Oppo, D. W., Ortega, P., Robson, J. I., Brierley, C. M., Davis, R.,
983 Hall, I. R., Moffa-Sanchez, P., Rose, N. L., Spooner, P. T., Yashayaev, I., and Keigwin, L.
984 D.: Anomalously weak Labrador Sea convection and Atlantic overturning during the past
985 150 years, *Nature*, 556, 227–230, <https://doi.org/10.1038/s41586-018-0007-4>, 2018.
- 986 Thrasher, B., Wang, W., Michaelis, A., Melton, F., Lee, T., Nemani, R. NASA global daily
987 downscaled projections, CMIP6. *Sci. Data* 9. [https://doi.org/10.1038/s41597-022-01393-](https://doi.org/10.1038/s41597-022-01393-4)
988 4, 2022.
- 989 Weertman, J.: The Theory of Glacier Sliding, *J. Glaciol.*, 5, 287303, 1964.
- 990 Weidick, A.: Historical fluctuations of calving glaciers in south and west Greenland,
991 *Rapp. Groenl. Geol. Unders.*, 161, 73–79. 1994.
- 992 Weidick, A.: Observations on some Holocene glacier fluctuations in West Greenland,
993 *Meddelelser om Grønland*, 165, 202pp., 1968.
- 994 Weidick, A., Bøggild, C. E., and Knudsen, N. T.: Glacier inventory and atlas of West
995 Greenland, 1992.
- 996 Weidick, Anker. and Bennike, Ole.: Quaternary glaciation history and glaciology of
997 Jakobshavn Isbrae and the Disko Bugt region, West Greenland : a review, *Geological*
998 *Survey of Denmark and Greenland*, 78 pp., 2007.
- 999 Yde, J. C. and Knudsen, N. T.: 20th-century glacier fluctuations on Disko Island
1000 (Qeqertarsuaq), Greenland, in: *Annals of Glaciology*, 209–214,
1001 <https://doi.org/10.3189/172756407782871558>, 2007.
- 1002 Young, N. E., Schweinsberg, A. D., Briner, J. P., and Schaefer, J. M.: Glacier maxima in
1003 Baffin Bay during the Medieval Warm Period coeval with Norse settlement, *Sci Adv*, 1,
1004 <https://doi.org/10.1126/sciadv.1500806>, 2015.
- 1005 Yu, L. and Zhong, S.: Changes in sea-surface temperature and atmospheric circulation
1006 patterns associated with reductions in Arctic sea ice cover in recent decades, *Atmos Chem*
1007 *Phys*, 18, 14149–14159, <https://doi.org/10.5194/acp-18-14149-2018>, 2018.
- 1008 Zekollari, H., Huss, M., and Farinotti, D.: Modelling the future evolution of glaciers in
1009 the European Alps under the EURO-CORDEX RCM ensemble, *The Cryosphere*, 13,
1010 1125–1146, <https://doi.org/10.5194/tc-13-1125-2019>, 2019.
- 1011 Zekollari, H., Huss, M., Schuster, L., Maussion, F., Rounce, D. R., Aguayo, R.,
1012 Champollion, N., Compagno, L., Hugonnet, R., Marzeion, B., Mojtabavi, S., and
1013 Farinotti, D.: 21st century global glacier evolution under CMIP6 scenarios and the role

<https://doi.org/10.5194/egusphere-2024-1770>

Preprint. Discussion started: 7 August 2024

© Author(s) 2024. CC BY 4.0 License.



1014 of glacier-specific observations, EGU sphere [preprint],

1015 <https://doi.org/10.5194/egusphere-2024-1013>, 2024.

1016